Three-dimensional Qp- and Qs-tomography beneath Taiwan orogenic belt: implications for tectonic and thermal structure

Yu-Ju Wang, Kuo-Fong Ma, Frederic Mouthereau, Donna Eberhart-Phillips

HAL Id: insu-03596891
https://insu.hal.science/insu-03596891

Three-dimensional *Qp*- and *Qs*-tomography beneath Taiwan orogenic belt: implications for tectonic and thermal structure

Yu-Ju Wang,[1] Kuo-Fong Ma,[1] Frederic Mouthereau[2,3] and Donna Eberhart-Phillips[4]

[1]*Institute of Geophysics, National Central University, Chungli, Taiwan. E-mail: fong@earth.ncu.edu.tw*
[2]*Institut des Sciences de la Terre et de l' Environnement de Paris, Université Pierre et Marie Curie – Paris 6, Paris, France*
[3]*Centre de Recherches Pétrographiques et Géologiques, Vandoeuvre-les-Nancy, France*
[4]*Geology Department, University of California, Davis, CA, USA*

SUMMARY

We determined the 3-D *Qp*- and *Qs*- structure of the Taiwan orogenic belt to enhance understanding of the related tectonic and thermal structure beneath the collision zone. The inversion used t^* values measured from the spectra of *P* and *S* waves from the dense Taiwan strong motion network for moderate size earthquakes (M_L 4.5–5.5) to avoid source complexity. The time period, 1991–2007, includes the aftershock sequence of the 1999 Chi-Chi earthquake that provides good ray coverage in central Taiwan. Over 18 000 velocity spectra from 883 earthquakes were analysed. A non-linear least square technique is applied to the spectra for t^* determination by assuming a ω^{-2} source model for the frequency band of 1–30 Hz. A frequency-independent *Q* was assumed in this study. The corner frequency of a specific event was fixed for the corresponding stations, and a quality index was defined to assure good quality data for the inversion.

The results reveal the sharp variation of *Qp* and *Qs* across the recently ruptured Chelungpu Fault, and the Kaoping and Chaochou Faults in Pingtung Plain. The *Q* values in the hangingwall are smaller by about 85 and 110 for *Qp* and *Qs*, respectively, relative to the footwall. The fault geometry is distinctly delineated by the contour of *Qp/Qs* of 1.2 that extends to the depth of the geologically identified décollement structure. Beneath the Central Range, the low *Qp*, low *Qs* and high *Qp/Qs* features coincide well with the aseismic zone. Comparison to the recent thermomechanical numerical models of Taiwan shows that the low *Q* zone corresponds to the exhumation of the lower crust. The low *Qs* regime (high attenuation) beneath the Central Ranges at the depth of 5–22 km coincides with predicted temperatures of 400–600 °C. The *Qs* comparison with the major tectonic and thermal mechanical models of Taiwan reveals that the shear wave attenuation model contains comprehensive rheological and thermal information of relevance to understanding mountain building processes. This technique appears particularly useful for distinguishing strong and weak crustal regions in the absence of other constraints.

Key words: Tomography; Body waves; Seismicity and tectonics; Seismic attenuation; Crustal structure.

INTRODUCTION

Taiwan is located at the collision boundary between the Philippine Sea Plate and the Eurasian Plate. In northeastern Taiwan, the Philippine Sea Plate is subducted below the Eurasian Plate, whereas in southwestern Taiwan the Philippine Sea Plate is overthrust onto the Eurasian Plate (Fig. 1a). In the highly seismic Taiwan area, numerous *Vp* and *Vs* tomographic studies have provided understanding of the mountain building processes, thanks to the high quality of local seismic data and the dense network (e.g. Rau & Wu 1995; Ma *et al.* 1996). More recently, Kim *et al.* (2005) conducted a tomography study for 3-D *P*- and *S*-wave velocity structures by combining data

sets from the Central Weather Bureau Seismic Network (CWBSN) and two temporary seismic arrays in Hualien and Pingtung (K.C. Chen 1995; K.P. Chen 1998). Arrival times from both local and teleseismic events have also been employed to achieve good resolution at greater depths (Wang *et al.* 2006). Based on a huge data set comprising 864 digital accelerographs in free field sites issued from the Taiwan Strong Motion Implementation Program (TSMIP) and deployed by the Taiwan's Central Weather Bureau (CWB), Wu *et al.* (2007) were able to provide high-resolution *Vp* and *Vp/Vs* tomography. Apart from the unpopulated high mountain areas, the TSMIP stations have achieved an average station spacing of a few kilometres. Fig. 1(b) shows the station distribution of the TSMIP
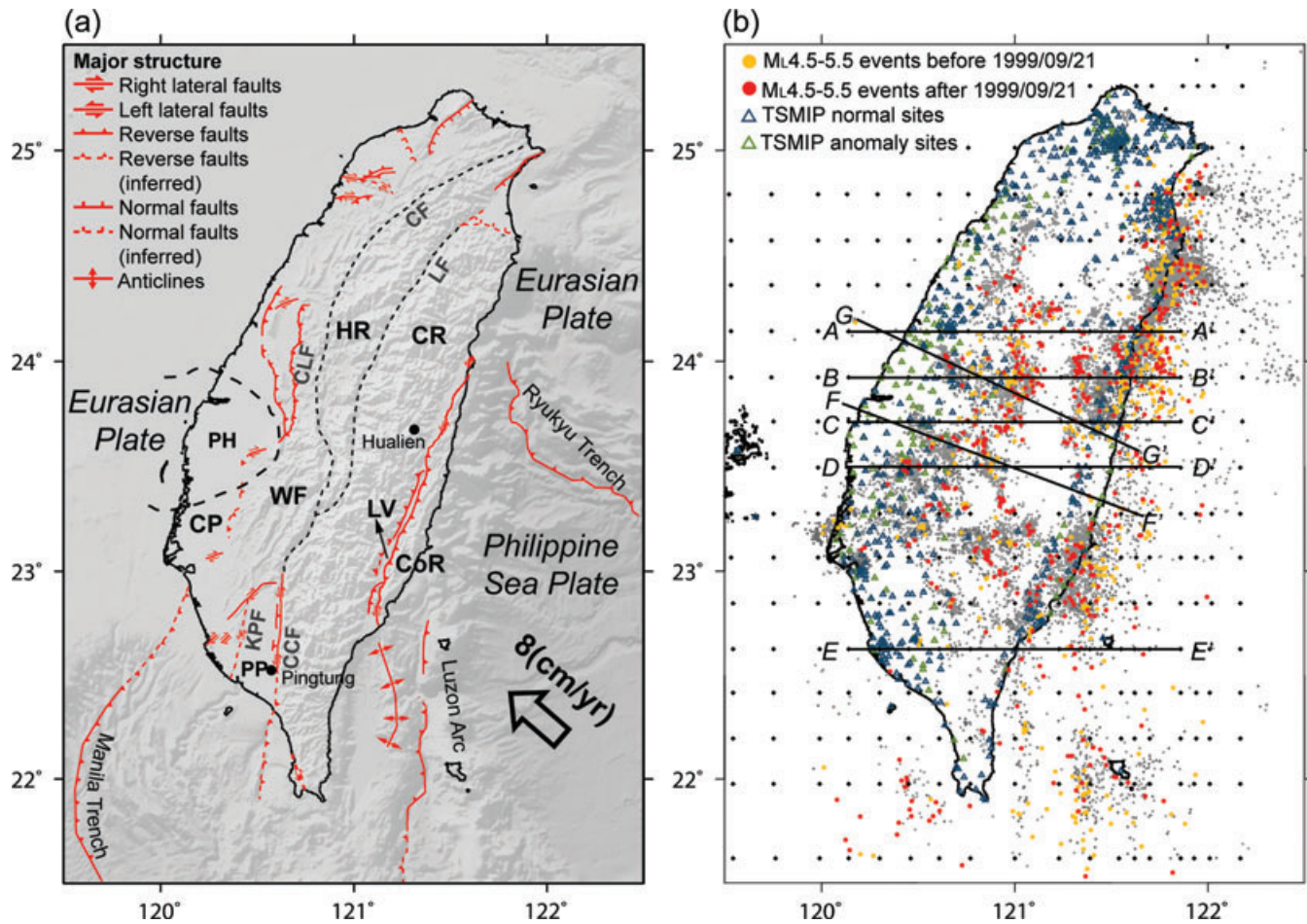
891

Figure 1. (a) The tectonic setting and distribution of the active faults in the Taiwan region, as denoted by the Central Geological Survey of Taiwan. The locations of the Ryukyu Trench to the east, the Manila Trench to the south and the Luzon Arc to the southeastern offshore Taiwan are indicated. The arrow shows the vector of relative motion between the Philippine Sea plate and the Eurasian plate with 8 cm yr^{-1} towards the northwest. Geological provinces are denoted by CP, Coastal Plain; WF, Western Foothills; HR, Hsuehshan Range; CR, Central Range; LV, Longitudinal Valley; CoR, Coastal Range and PP, Pingtung Plain. The Peikang High (PH) structure was denoted by Hsu *et al.* (2008).The types of faulting and folding identified by Shyu *et al.* (2005) are represented with different symbols. The red solid lines indicated the identified active faults and folding, the red dashed lines indicate the inferred active faults. The significant identified active faults are CLF, Chelungpu Fault; KPF, Kaoping Fault and CCF, Chaochou Fault. The Chuchih Fault (CF) and Lishan Fault (LF) that delineate the boundaries of the Western Foothills, Hsuehshan Range and the Central Range, respectively, are shown by black dashed lines. (b) Distribution of the selected events of with M_L 4.5–5.5 in this study and the grids (diamond) used in the modelling. The orange and red dots present the events before and after the occurrence of the 1999 Chi-Chi earthquakes, respectively. The background seismicity recorded by Taiwan Strong Motion Implementation Program (TSMIP) in 1991–2007 is indicated by the grey dots. The blue triangles are the stations from TSMIP used in this study, whereas the stations in green triangles have strong site effects and so are excluded in this study. The model gridding was set with grid size of 8–24 km in the longitudinal direction and 24 km in the latitudinal direction. The profiles referred in this studies as *AA′–EE′* are shown, which are located at the latitude of 24.2°N, 23.9°N, 23.7°N, 23.5°N and 22.6°N, respectively. Section *FF′* is oriented N110°E and section *GG′* is oriented N115°E.

network. During the past 15 yr, a large number of high-quality digital accelerograms have been recorded from tens of thousands of earthquakes of magnitudes $M_L = 2$–7, especially the massive data set since the 1999 Chi-Chi (M_w 7.6) earthquake sequence.

In contrast to the numerous studies of *Vp* and *Vp/Vs* tomography, for the important geophysical parameter of seismic attenuation, there is a relative lack of studies for constraining the deep 3-D structure of the Taiwan collision belt. The earlier *Qp* and *Qs* tomography studies carried out by Chen *et al.* (1996) and Chen (1998) had only 75 stations over the island of Taiwan from the Taiwan Telemetered Seismographic Network (TTSN) and CWBSN data. Due to the few available seismic stations and lack of earthquakes beneath the Central Range (CR) during their study period, their low-resolution results provide little constraint on structural features.

In this study, we compute a 3-D *Qp* and *Qs* model using the seismic waveform data from the dense TSMIP data of 864 stations, restricted to the frequency range of 1–30 Hz. The *Vp* and *Vs* tomography has informed several tectonic models of Taiwan orogeny. The main advantage of performing a 3-D *Qp* and *Qs* model is to provide additional insights on rock properties suffering the effect of temperature, fluid, fracture, permeability and porosity, for these properties have a relatively greater effect on attenuation than velocity. These geophysical characteristics can provide additional constraint to the competing tectonic models of Taiwan. We will particularly focus on the *Qs*, which is more sensitive than *Qp* to temperature and fluid contents in rocks. The discrepant variation in *Qp* and *Qs* related to different elastic attenuation modes also makes the *Qp/Qs* ratio a particularly sensitive indicator for rock conditions.

In terms of tectonics of the Taiwan region, several key features have been inferred but not yet well explained. For instance, a low velocity zone beneath the CR has been observed in many studies at depths of 20–40 km based on *P*- and *S*-wave tomography (Roecker *et al.* 1987; Rau & Wu 1995; Ma *et al.* 1996; Kim *et al.* 2005; Wu *et al.* 2007). Kim *et al.* (2005) inferred that this low velocity corresponded to ductile material contrasting with the brittle, higher-velocity material at depths shallower than 15 km. Thermal modelling of heat flow data also supported the occurrence of an aseismic and higher-temperature belt beneath the eastern CR (Lin 2000). Recent numerical models of the Taiwan collision have successfully reproduced such a thermal anomaly beneath the CR, although the origin is still being debated (Simoes *et al.* 2007; Yamato *et al.* 2009). In addition to the heat flow data, Bouguer gravity anomalies showed that there is no negative anomaly under the CR (Hsu *et al.* 1998; Yen *et al.* 1998). This suggests that there is no root beneath the CR so that it is not compensated isostatically. Alternatively, this result could be interpreted as reflecting the presence of dense material involved in shortening beneath the CR, for instance, it could be compatible with the squeezed lower crust that was suggested by recent modelling (Yamato *et al.* 2009).

In an attempt to describe the Taiwan mountain building process, several geodynamic models have been proposed over the past three decades (e.g. Suppe 1981; Chemenda *et al.* 1995; Wu *et al.* 1997; Lin *et al.* 1998; Malavieille *et al.* 2002; Simoes *et al.* 2007; Yamato *et al.* 2009). Although each model has a different geodynamic implication, they can be divided into two end-member models (e.g. Mouthereau & Lacombe 2006). The thin-skinned or subduction model considers Taiwan as the product of continuous subduction of the Eurasian Plate (i.e. crust and mantle lithosphere) beneath the Taiwan Island (e.g. Suppe 1981; Malavieille *et al.* 2002; Simoes *et al.* 2007). According to this thin-skinned model, orogenic contraction is accommodated above a main basal seismogenic detachment located in the crust, that climbs upsection to be finally emergent at the western belt front. Because this model implies the subduction of Eurasian material, the lack of seismogenic shortening in the CR is interpreted as resulting from the ductile underplating of the upper Eurasian crust beneath the Taiwan main décollement (e.g. Simoes *et al.* 2007).

An alternative, thick-skinned or collision model predicts that Taiwan is growing within and onto the Eurasian Plate, although the amount and processes by which the continental crust is accreted can be different (Chemenda *et al.* 1995; Wu *et al.* 1997; Lin *et al.* 1998; Yamato *et al.* 2009). In this category of model (e.g. Wu *et al.* 1997; and Yamato *et al.* 2009), the aseismic zone beneath the CR is interpreted to be associated with the frontal accretion of the thermally weakened middle–lower crust forming a thick wedge of Eurasian material. In this case, the subduction of the Eurasian crust is very limited.

DATA AND METHOD

Here, we have considered the earthquakes recorded by the Taiwan Strong Motion Network for the time period of 1991–2007 with magnitudes M_L 4.5–5.5, to avoid source complexity. In total, 971 events were chosen, of which 618 events were after the 1999 September 21 Chi-Chi (M_w 7.6) earthquake. Fig. 1(b) shows the distribution of the events recorded by the CWB during the studied time period and the events selected for the *Q* tomography study. We consider all types of available data recorded by the Taiwan Strong Motion Network (Fig. 1b) for these events, except for the stations that had

shown anomalously strong site effects (Wen *et al.* 2005). The instruments have the dynamic ranges of 12, 16 or 24-bit FBA sensor with good resolution of the frequency response from dc to 50 Hz for the sampling rate of 200 or 250 points per seconds.

For identifying the *P* and *S* waves, we employed the well-developed STA/LTA algorithms (Allen 1978) for automated body wave determination. We considered two consecutive moving time windows, the short-term average (STA) as the instantaneous amplitude of the seismic signal and long-term average (LTA) as the average seismic noise (Trnkoczy 1998). The STA/LTA ratio is continuously compared with the selected trigger threshold level. We considered a time window of 0.2 s for STA and 5 s for LTA for a moving window along the digital record. When the ratio exceeded the threshold value of 5, the *P*-wave arrivals were identified. A 2.5 s time window after *P* wave, as is adequate duration for phase energy for M_L 4.5–5.5 events, was examined for the spectra analysis. The *S* wave was picked for 0.2 s of STA, 2 s of LTA and threshold value 2 and a 4.5 s time window for spectra analysis. Fig. 2 shows one example for an event of magnitude 5.1 recorded by station HWA035, and the STA and LTA durations used in this study. After the STA/LTA identification, all records were again examined manually to avoid the occasional mistakes from autopicking. The acceleration records were integrated once to velocity for the frequency domain analysis. The velocity spectra of the selected time-window records after *P* or *S* arrivals were investigated for t^* estimation. A background noise spectra, which is 0.5 s before arrivals with the same duration (Fig. 2), was also investigated for qualifying the values of t^* with respect to the signal-to-noise ratio (*S/N*).

t^* ESTIMATION FOR Qp AND Qs TOMOGRAPHY

The observed velocity spectra $A_{ij}(f)$, for the event *i* to the station *j*, was modelled by ω^2-source model with the assumption that the *Q* is independent of frequency, it follows,

$$A_{ij}(f) = 2\pi f \Omega_0 \frac{f_c^2}{f_c^2 + f^2} \exp(-\pi f t_{ij}^*)$$

(Scherbaum 1990; Eberhart-Phillips & Chadwick 2002), where Ω_0 is the long-period plateau value, f_c is the corner frequency and t_{ij}^* is whole path attenuation operator. Each of the velocity spectrum was fitted by non-linear least-squares (LSQENP) method (Marquardt 1963) in the frequency band of 2–30 Hz for *Qp* and 1–20 Hz for *Qs* to obtain the values of Ω_0, f_c and t_{ij}^* for each ray path of event *i* to the station *j*. Because the corner frequency is a source parameter that should be constant for every individual event recorded at all stations, two steps in the non-linear least square analysis were utilized for the determination of t_{ij}^*. First, we obtained the values of Ω_0, f_c and t_{ij}^* for every individual ray path by minimizing the residuals of observed and theoretical spectrum. Then, for every individual event, a corner frequency was obtained by averaging the value of the f_c recorded by the corresponding stations of this individual event. Thus, the obtained f_c is fixed for the second step of the LSQENP, for estimation of t_{ij}^*. For our magnitudes, the appropriate f_c range is less than 10 Hz, following the seismic scaling law (Aki 1967; Geller 1976). Thus, we only consider averaging the f_c values between 1 and 10 Hz for coincident records of an individual event. Most of the events have corner frequency of 3–7 Hz estimated by *P*-wave spectra (f_c^p) and 2–5 Hz by *S*-wave spectra (f_c^s) (Fig. 3), which are comparable to the theoretical values (Drouet *et al.* 2005) for earthquakes of M_L 4.5–5.5. Instead of being equivalent, f_c^p are
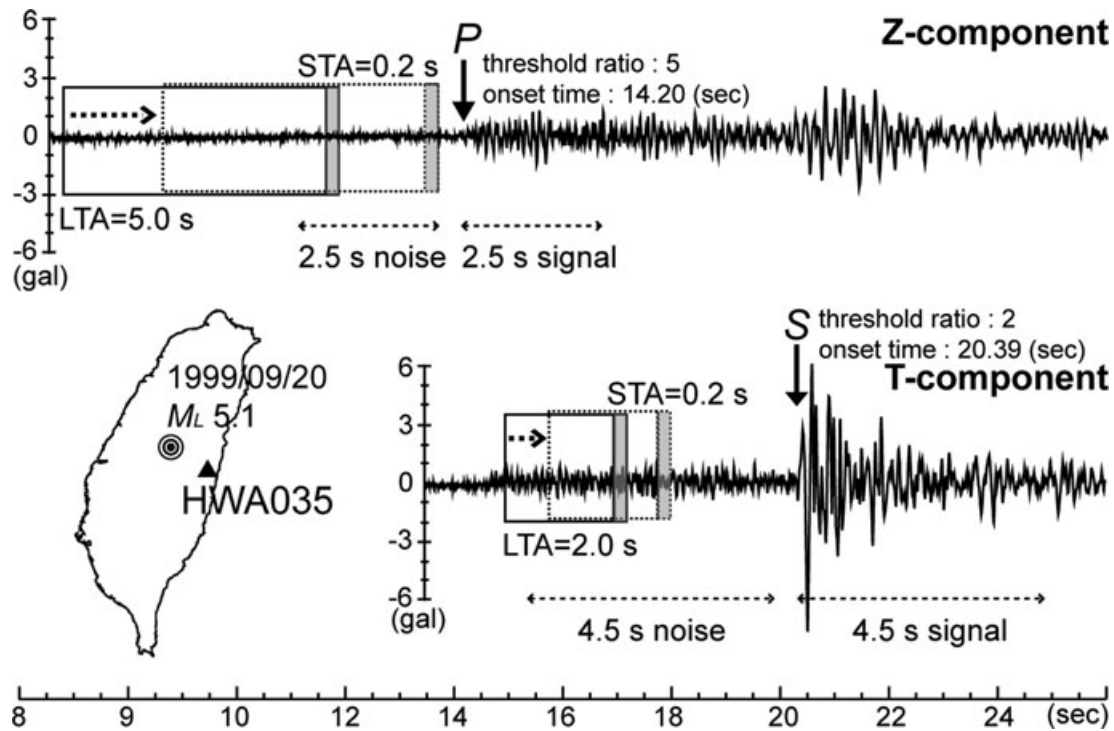
Figure 2. The diagram shows the criteria for data processing. The scheme of short-term average (STA) over the long-term average (LTA) algorithm with relating parameters is shown. The example shows the distinct waveforms of the 1999 September 20 event ($M_L = 5.1$) recorded by station HWA035 located in the eastern Taiwan. The locations of the event (multiple circles) and station HWA035 (triangle) are also shown. The *P*-wave signal was picked up at 14.20 (s) on the Z-component (top panel) by sequentially comparing the ratio of STA in 0.2 s of time window (grey shaded area) and LTA with 5 s of time window (rectangle block) to achieve the threshold value 5. Then, a 2.5 s time window after onset time of the *P* wave (dashed line) was adopted for estimating t^* with noise spectrum having the same time duration before 0.5 s of *P* wave (front dashed line). Right-hand bottom panel shows that the *S* wave was picked up at 20.39 (s) on the T-component with threshold value 2. The 0.2 s STA duration of *S* wave (grey shaded area) is the same as for the *P* wave, but the LTA window is 2 s (rectangle block). The horizontal dashed lines indicate the time window of the *S* wave and noise as 4.5 s.
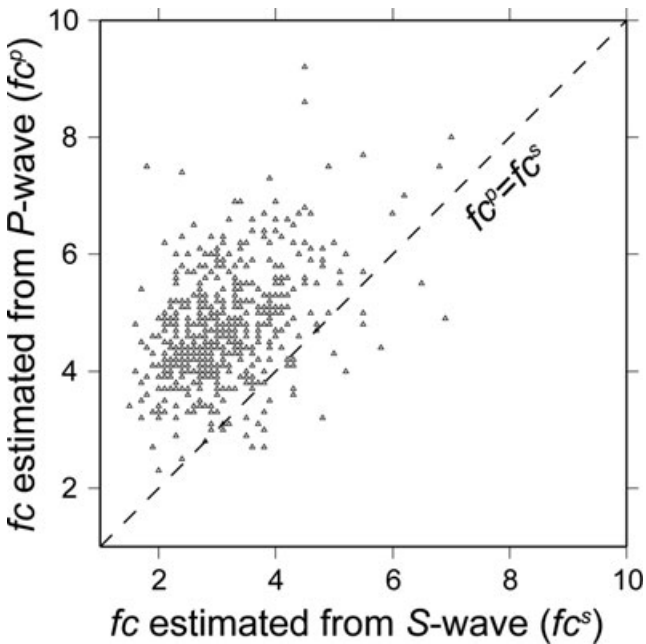

Figure 3. The relationship of determined corner frequency (f_c) from *P* and *S* wave of data events. The dashed line represents an f_c estimated by *P*-wave spectra (f_c^p) equal to the one estimated by *S*-wave spectra (f_c^s). The f_c values (triangles) were virtually all located above the dashed line.

larger than f_c^s, although this has little influence for estimating Q values.

To ensure the quality of the inversion for Q, the data quality index (Q.I.) has been assessed by two factors: the N/S index (NSI), based on the percentage of the high quality *S/N* in the entire fitting spectra, and the misfit factor, which is the deviation of observed and predicted spectrum in the spectrum fitting by LSQENP. The NSI was defined by how much of the percentage of duration has the *S/N* higher than 4.5 within the entire fitting *P*-wave spectrum and 2.3 within the *S*-wave spectrum. The values of 4.5 and 2.3 were obtained empirically as values that differentiate the signal quality without misjudgment over the duration of the time window. The NSI is set to be 0.0 if more than 80 per cent in the analysed spectrum has *S/N* > 4.5 for *P* wave and 2.3 for *S* wave. The NSI are 0.5, 1.0, 1.5 and 2.0, respectively, for 70, 60, 40 and <40 per cent as indicated in Table 1. For every individual t_{ij}^*, the Q.I. was determined through the summation of the NSI value and misfit factor to give the weight to the t_{ij}^* for inverting Q tomography. Q.I. is 0 for excellent data having the sum equal 0, and 1 or 2 for the sum less than 1.0 or 2.0, respectively. For the sum larger than 2.0, t_{ij}^* data is discarded in this study. Fig. 4 shows the examples of spectra fitting and their Q.I. for the event on 2000 September 1, M_L 4.9 recorded by the surrounding stations.

In total, there are 18 006 t_p^* (t_{ij}^* estimated by *P* wave) and 19 270 t_s^* (t_{ij}^* estimated by *S* wave) for 815 events used for inverting the Q_p and Q_s tomography. Table 2 shows the evaluated Q.I. values of

Table 1. The list of the related parameters for definition of the N/S index (NSI).

Quality	D: duration in 2–30 Hz of signal-to-noise ratio > 4.5 for Qp (in 1–20 Hz of signal-to-noise ratio > 2.3 for Qs)	NSI
Best	$D \geq 80$ per cent	0.0
	80 per cent $> D \geq 70$ per cent	0.5
↓	70 per cent $> D \geq 60$ per cent	1.0
	60 per cent $> D \geq 40$ per cent	1.5
Bad	40 per cent $> D$	2.0

Notes: The spectrum for *Qp* and *Qs* were analysed for the frequency of 2–30 Hz and 1–20 Hz, respectively. The t^* quality (left) is related to the duration percentage (*D*) of signal-to-noise ratio larger than 4.5 for *Qp* and 2.3 for *Qs* (centre). For *D* more than 80 per cent, the NSI (right) is set to 0.0. And NSI is set to be 0.5, 1.0, 1.5 and 2.0, respectively, for *D* larger than 70, 60, 40 and less than 40 per cent. Table 1. Definition of N/S index (NSI).

t_p^* and t_s^* used in this study. Most of the t_{ij}^* have Q.I. values with 1. Fig. 5 shows the t_{ij}^* distribution for four events in the central and southwestern Taiwan. These t_{ij}^* distributions show the general increase of t_{ij}^* values with the epicentral distance. However, anomalies are detected around western central Taiwan where the Peikang High (PH) as denoted. The smaller t_{ij}^* value implies lower attenuation in this region.

The value of t_{ij}^* can be expressed as $t_{ij}^* = \int_s \frac{1}{Q(x,y,z)\,V(x,y,z)}\mathrm{d}s$, where $Q(x, y, z)$ and $V(x, y, z)$ are the quality factor and the velocity structure along the ray path from the event *i* to the station *j*. Assuming the resolved velocity structure $V(x, y, z)$, the *Q* structure can be obtained through the estimation of the t_{ij}^*. In this study, we followed the algorithm of simul 2000 developed by Thurber & Eberhart-Phillips (1999) to image 3-D *Qp* and *Qs* values of the whole Taiwan area, incorporating the well-resolved *P*- and *S*-wave velocity tomography of Kim *et al.* (2005). The 3-D velocity is useful for computing ray paths, however small differences in velocity have little effect on *Q* because *Q* variation can be large, up to a factor of 10.

MODEL AND RESOLUTION OF *Q* TOMOGRAPHY

The 3-D grid used for the *Q* tomography is defined by considering the ray path density among events and stations. Because most of the stations and events are located in eastern and western Taiwan, the grid spacing is smaller there than in the CR to keep similar ray path density in each block. The final grid is shown in Fig. 1(b). The grid spacing for inland Taiwan ranges from 8 to 24 km in the longitudinal direction and 24 km in the latitudinal direction. The Coastal Plain (CP) and the Western Foothills (WF), with numerous stations, have a 16-km-width grid, whereas in northeastern Taiwan we considered an 8-km-width grid for the abundant earthquakes. The grid setting in the vertical direction is set to follow the velocity model to diminish the interpolation error. As a result, the depths chosen were set at 1, 5, 9, 19, 27, 39, 55, 81, 147 and 200 km, respectively, in agreement with Kim *et al.* (2005). The *Qp*, *Qs* values with depth evaluated by Chen *et al.* (1996) and Chen (1998) were adopted for initial *Qp* and *Qs* model (Fig. 6) in our 3-D *Q* tomography.

The resolution of our *Q* distribution was determined from the spread function in the inversion. The spread function (SF) as defined

by Michelini & McEvilly (1991) is given by

$$\mathrm{SF}_j = \log\left[|r_j|^{-1} \sum_{k=1}^{N} \left(\frac{r_{kj}}{|r_j|} \right)^2 D_{jk} \right],$$

where SF_j is the spread function of the *j*th gridpoint, r_{kj} denotes elements of corresponding resolution matrix and D_{jk} denotes the weighting factor related to the distance to each element. The SF shows the smearing from other gridpoints, and the smaller value of the spread function shows that the *j*th node *Q* value is more independent of adjacent nodes. According to Toomey & Foulger's (1989) criterion, SF = 4.5 is chosen as the maximum acceptable SF value for our *Q* images resolution. The resolution of the *Q* model is also related to the ray density that can be quantified by calculating the derivative weight sum (DWS). As shown in Fig. 7, the logarithm of DWS has a linear relationship with the SF. After analysing, SF = 4.5 in this study, the correlated DWS is 780 in *Qp* and 480 in *Qs*. In our acceptable resolution grids (SF ≤ 4.5), there are about 62 grids (i.e. 16.7 per cent) with DWS < 780 in *Qp* nodes, and 69 grids (i.e. 12.8 per cent) with DWS < 480 in *Qs* nodes.

The image resolution is limited in the CP, where it is restricted by availability of crossing rays, with fewer events in western offshore Taiwan. In contrast, the model is well resolved in eastern and southeastern Taiwan thanks to numerous events distributed in the eastern offshore areas. Most of our resolution is above the depth of 39 km. Below this depth, there is little resolution because of fewer observation data.

RESULTS

The final rms residuals of the inverted *Qp* and *Qs* tomography are 0.017 and 0.009 with variance of 0.00029 and 0.00088, respectively, which are similar to the studies of Eberhart-Phillips & Chadwick (2002). There are 99 and 94 per cent nodes of the resolvable model of *Qp* and *Qs* (SF ≤ 4.5), respectively, within the standard errors of less than 50. Considering the resolution of the results, only the *Qp* and *Qs* tomography from 0 to 39 km depth are interpreted, where the images have the resolution of SF ≤ 4.5.

3-D *Qp* tomography

Fig. 8 shows the results of the *Qp* tomography, with the corresponding distribution of SF ≤ 4.5. At the top 1 km depth, a reliable resolution for interpretation is found mainly in the WF, and the resolution in the CR is relatively poor, due to the lack of data (Fig. 8a). Significant variation of *Qp* is found across the Chelungpu Fault (CLF), with lower *Qp* in the hangingwall than that in the footwall (Fig. 8a). Even though this is a small-scale feature, the across-fault *Qp* contrast extends prominently to 5–9 km depth (Figs 8b and c). In the WF, *Qp* values from latitude 23°N to 24.2°N are relatively low at 1–5 km depth (Figs 8a and b), which corresponds to low *Vp* and low *Vp/Vs* features (Wu *et al.* 2007) relative to the CP. These results imply that the WF contains partially water-saturated sediments as compared to the fully saturated alluvial in the CP (Winkler & Nur 1982; Walsh 1995).

At 9 km depth, two distinct high *Qp* zones were observed in the northern and southern CR and bounded in the west by the longitudinal valley (LV) (Fig. 8c). In contrast to these two high *Qp* regimes, there is a low *Qp* belt trending obliquely in the NW–SE direction. In southern Taiwan, for the region beneath Pingtung Plain (PP), low *Qp* was imaged distinctively at 9–19 km depth (Figs 8c and d).
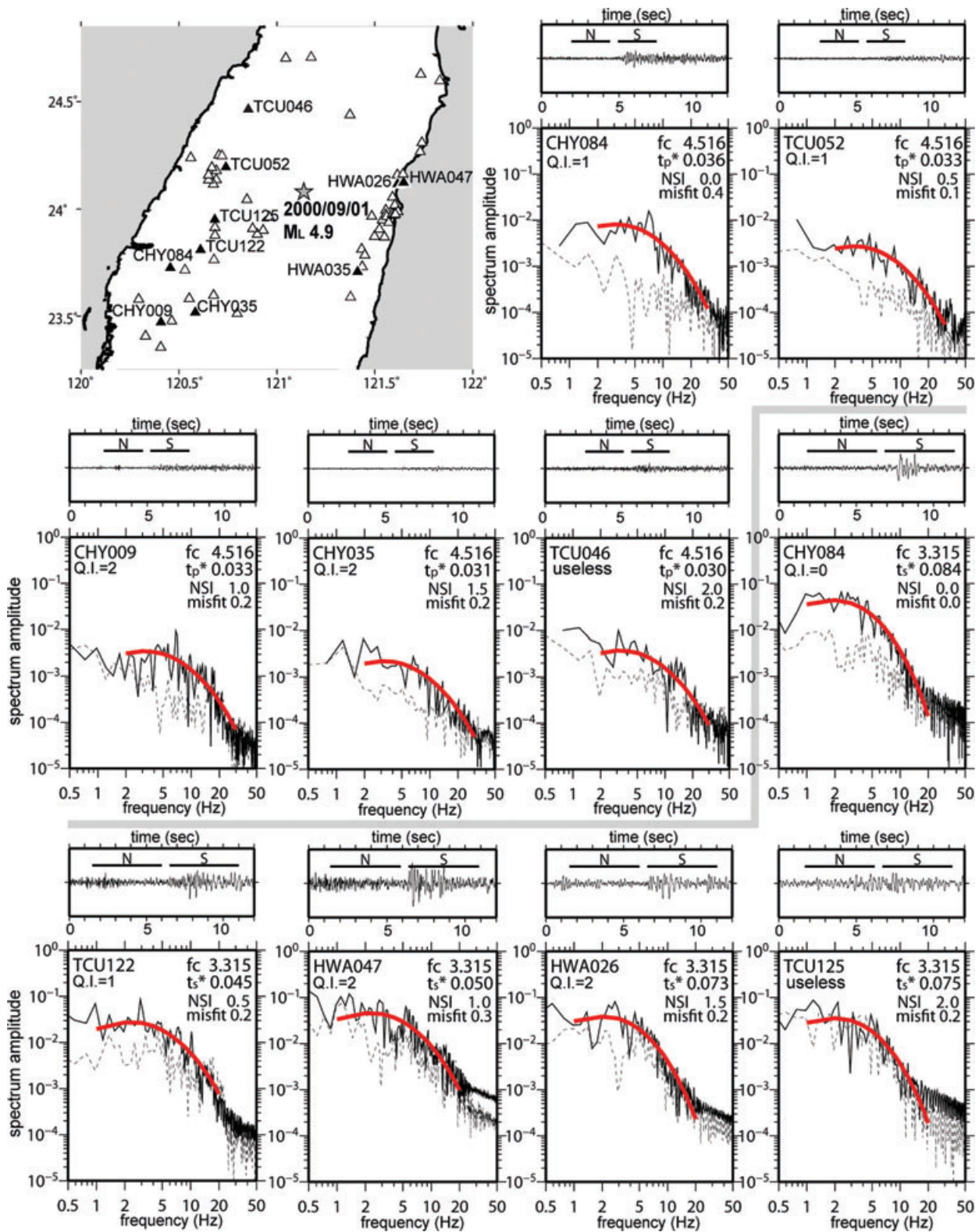
Figure 4. 10 examples of spectra fitting and their Q.I. for the event of 2000 September 1 ($M_L = 4.9$) recorded by the surrounding stations. The distribution of the stations (triangles) for the event (star) is shown in the map at the left-hand top corner. The spectra of the stations denoted by the solid triangles are shown. The top five spectra are for the *P* wave and the bottom five ones are for the *S* wave, respectively, separated by the grey line. Each spectrum has its adopted time interval for the signal (*S*) and noise (*N*) shown above. The estimated curve of non-linear fitting is shown in heavy red line and the dashed line shows the noise spectrum. Its determined corner frequency (f_c), t^* value (t_p^* for *P* wave; t_s^* for *S* wave), N/S index (NSI) and misfit factor are also shown in the right-top corner of each panel. The corresponding station name of each spectrum and resulted quality index (Q.I.) are marked in the left-top corner. Q.I. is 0 for excellent data for the sum of NSI and misfit equals 0. Q.I. of 1 and 2 are for the sum less than 1.0 and 2.0, respectively. The sum of NSI and misfit as larger than 2.0, data were rejected in our study.

Table 2. The table summarizes the quality (Q.I.) of data used in the Taiwan Q tomography, listing the total number of t_p^* and t_s^* for the Q.I. of 0, 1 and 2.

Q.I.	Number of t_p^*	Number of t_s^*
0	80	192
1	15 841	15 892
2	2085	3186
Total	18 006	19 270

In the lower crust, at 19 km depth, the high Qp features seen at 9 km depth are now more distinct (Fig. 8d). At this depth, the high Qp zone extends eastward to offshore Taiwan, and further south is aligned with the strike of the Luzon Arc. In western Taiwan, a significant high Qp feature to the east of the CLF and west of the Lishan Fault (LF) was identified. This feature extends deepest beneath the Hsuehshan Range (HR), to at least 27 km depth, which is the extent of our resolution. In contrast to this high Qp zone, a distinct low Qp zone under the CR at lat. 23.5°N–24°N was observed. In eastern Taiwan, a high Qp zone was observed along the Coastal Range (CoR) at 27 km depth (Fig. 8e). At 39 km depth, the Qp

image is not sufficiently resolved to provide a reliable interpretation (Fig. 8f).

3-D Qs tomography

The patterns of the spatial Qs variations for each layer (Fig. 9) are very similar to the patterns observed in the Qp images, but with more distinct features. Because the high seismicity of Taiwan allows us to limit data to $5.5 \geq M_L \geq 4.5$, Qs is well observed and has better spatial resolution than Qp, as illustrated by SF (Fig. 9). The relatively high attenuation feature (low Q) found in the hangingwall of the CLF was also confirmed in the Qs images within the depth range of 1–9 km (Figs 9a–c), and is now more clearly aligned with the CLF than that in Qp images. In the PP, in addition to the low Qp appearing at the depth of 9 km, a low Qs feature was also imaged extending to shallower depths of 1–5 km (Figs 9a and b). Similarly, to the low Qp, the low Qs of PP also extends to 19 km depth (Fig. 9d). The high Qs features at the depths of 9–19 km are similar to those observed in Qp, although the high Qp features have higher values than those for Qs. The high attenuation zone, striking across northwestern to southeastern central Taiwan and to the CoR, also
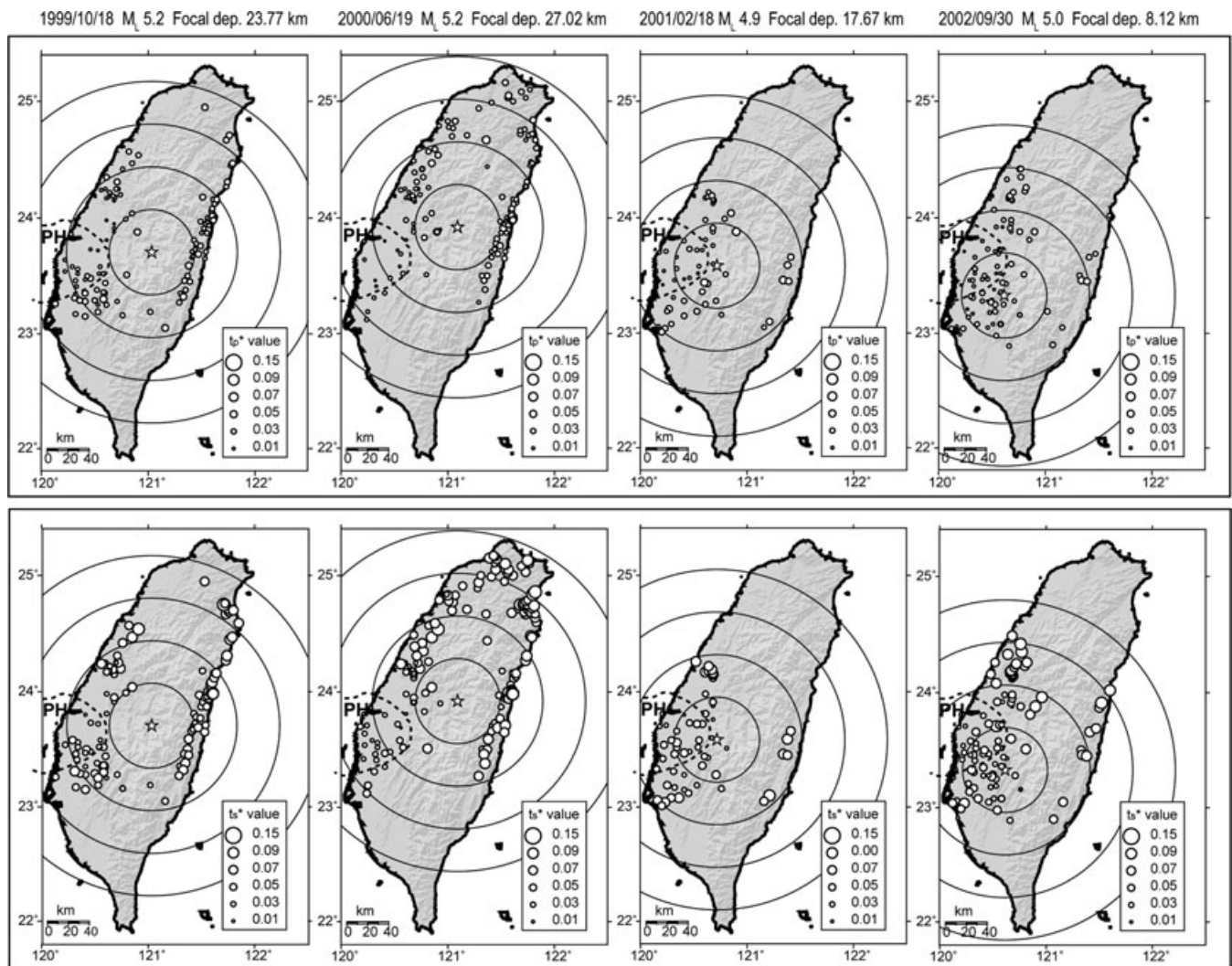

Figure 5. Examples of t_p^* (top panel) and t_s^* (bottom panel) distributions for four selected events, which were recorded by more than 100 TSMIP stations. The star shows the location of the event and the radii of the equal epicentral distances are shown with the increment of every 40 km. The tectonic structure of Peikang High (PH, Hsu *et al.* 2008) is denoted by dashed circle.
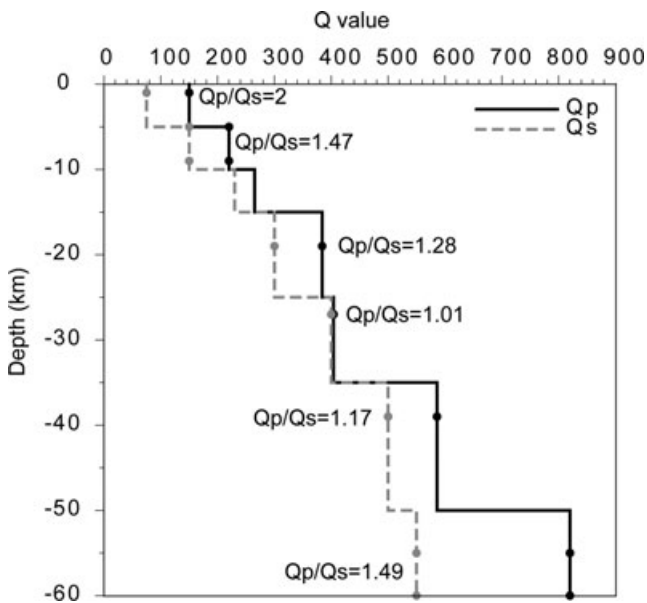
Figure 6. The initial models of *Qp* (solid line) and *Qs* (dashed line), obtained from the *Q* model of Chen (1996, 1998). The ratios of the corresponding values of *Qp* to *Qs* are also presented. The dots represent the initial *Qp* and *Qs* values adopted for our initial models at different depths.

separates the high *Qs* features (Fig. 9c). At 19 km depth, the low *Qs* feature beneath the CR is more pronounced than that in *Qp*. An additional low *Qs* feature was found north of the HR along strike, and is bounded by two fault systems. In northern Taiwan, the *Qs* image is more detailed than the *Qp* due to improved resolution.

A high *Qs* feature similar to that observed in *Qp* tomography was obtained around the latitude of 24°N at the depth of 27 km (Fig. 9e). Even with the improved spatial resolution, this high *Qs* feature has the same compact shape with a sharp southern boundary at 23.5°N. The high *Qs* feature extends to 39 km depth (Fig. 9f), but the resolution is not sufficient to interpret its shape at that depth.

The massive data set with good spatial coverage allows us to resolve more distinct tectonic features than the previous attenuation models (Chen *et al.* 1996; Chen 1998), such as the anomaly across the CLF, the PP low *Q*, the high attenuation zone under the CR at latitude 23.5°N–24°N at 19 km depth and the low attenuation along the Luzon Arc or CoR at 19 and 27 km depth, respectively. These high-resolution attenuation features provide more constraints for understanding tectonic features, especially the correspondence to the thermal history.

DISCUSSION

To compare the results with the tectonic structure, we make the profiles *AA′* to *CC′* and *EE′* for *Qp*, *Qs* and *Qp/Qs*, respectively (Figs 10 and 11). The profiles for *Qp/Qs* are helpful to understand the possible interpretation of the features. Note that the 1-D initial model (Chen *et al.* 1996; Chen 1998) had *Qp/Qs* = 2 in the upper 5 km and *Qp/Qs* of 1.0–1.5 in the layers below 5 km depth. The locations of the profiles are shown in Fig. 1(b). The profile *AA′* is at the latitude of 24.2°N across the recently ruptured CLF. The profiles *BB′* and *CC′* are at latitudes 23.9°N and 23.7°N, respectively, across the aseismic zone beneath the CR (Wang *et al.* 1994; Ellwood *et al.* 1996; Ma *et al.* 1996; Lin 1998). The profile of *EE′* is across the PP.
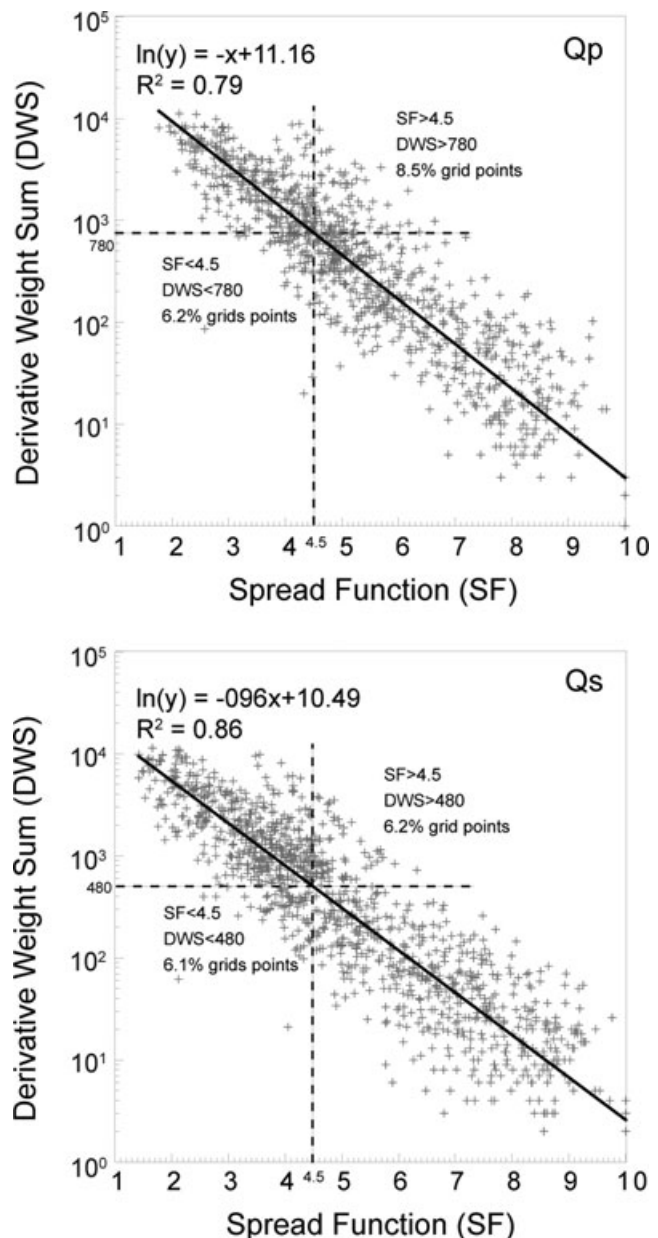

Figure 7. The statistical chart of derivative weight sum (DWS) and spread function (SF) values of each model parameters for *Qp* (top panel) and *Qs* (bottom panel). The linear relationship between the logarithm of DWS and SF values were obtained by the linear fitting shown with the regression equation and R-square. The four quadrants (dashed line) were defined for SF of 4.5 and DWS of 780 for *Qp*, and SF of 4.5, and DWS of 480 for *Qs*, respectively. The percentage of the data that satisfied the condition in the first and third quadrant are also denoted for reference.

To aid tectonic interpretation, we carried out synthetic tests to examine the spatial resolution of significant features (see Appendix A). The synthetic test models had some simple shapes to examine (1) the sharp variation across the CLF, and KPF and CCF, which bound the PP at 1–19 km depth; (2) the low *Qs* of the aseismic zone at 19 km depth and (3) high *Qs* features at the depths of 27 and 39 km. In synthetic test model I (Fig. A1), the low *Qs* (*Qs* = 50) features were set east of CLF at 1–9 km depth and the aseismic zone under CR at 19–27 km depth. In southwestern Taiwan, the synthetic model also has a low *Qs* in the PP bounded by KPF and
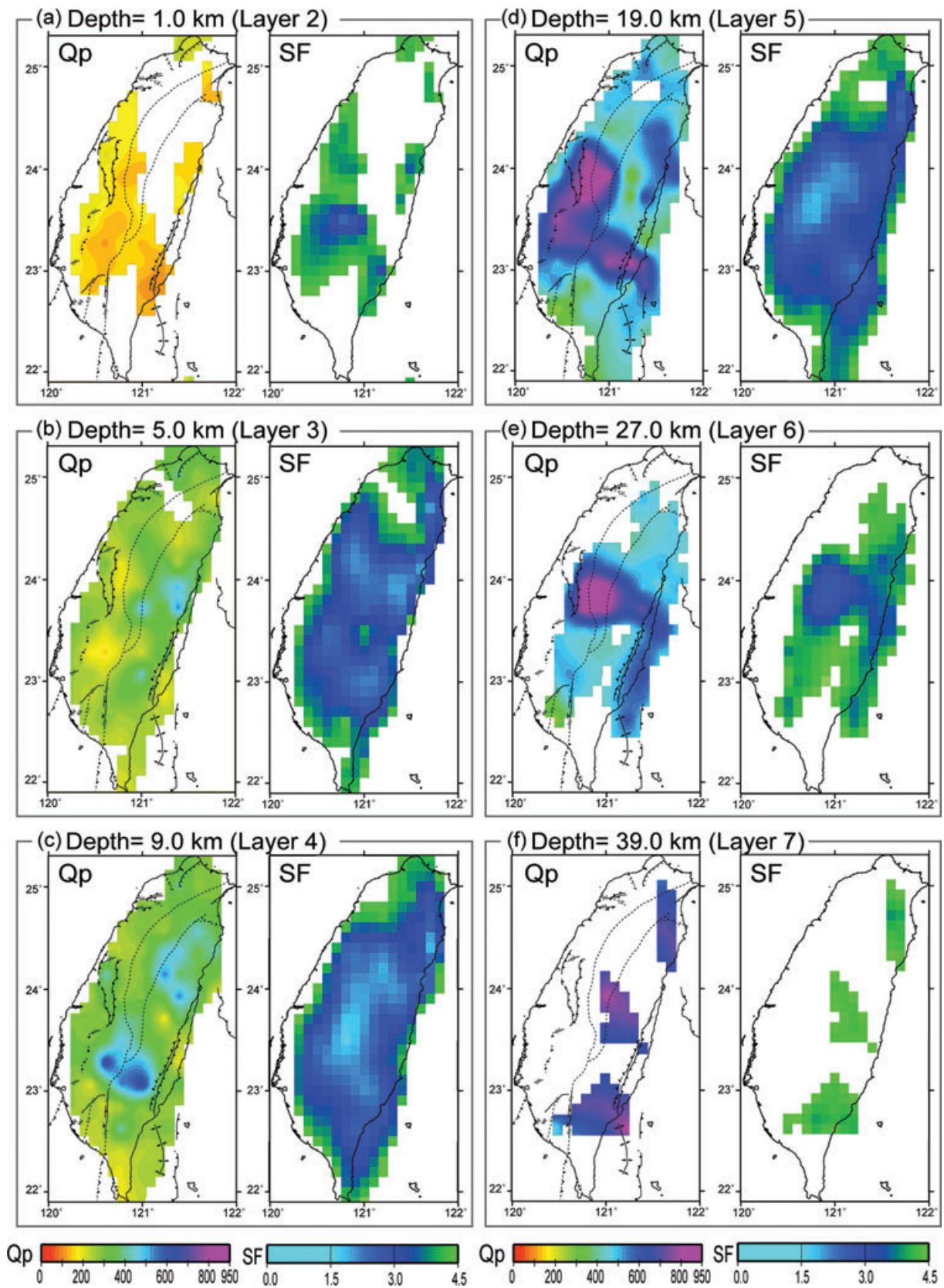
Figure 8. The 3-D inverted *Qp* tomography with SF ≤ 4.5 at the depths of 1, 5, 9, 19, 27 and 39 km. The corresponding spread function (SF) at each depth is also shown. Colour bars of *Qp* and SF (bottom panel) show the corresponding value in images. The major tectonic features are shown, following Fig. 1(a).

Figure 9. The three-dimensional inverted Qs tomography with SF ≤ 4.5 at the depths of 1, 5, 9, 19, 27 and 39 km. The corresponding spread function (SF) at each depth is also shown. Colour bars of Qs and SF (bottom panel) show the corresponding value in images. The major tectonic features are shown, following Fig. 1(a).
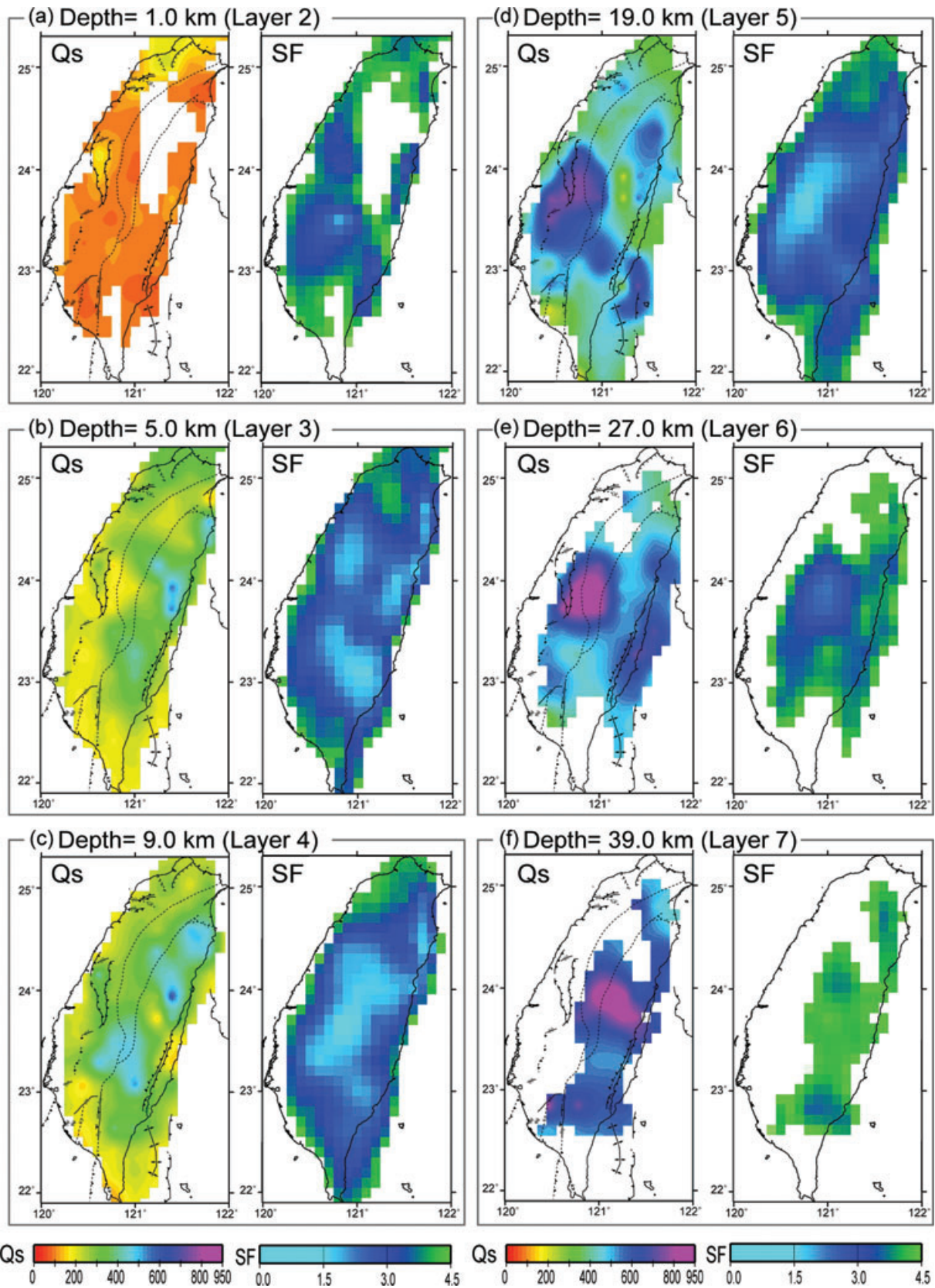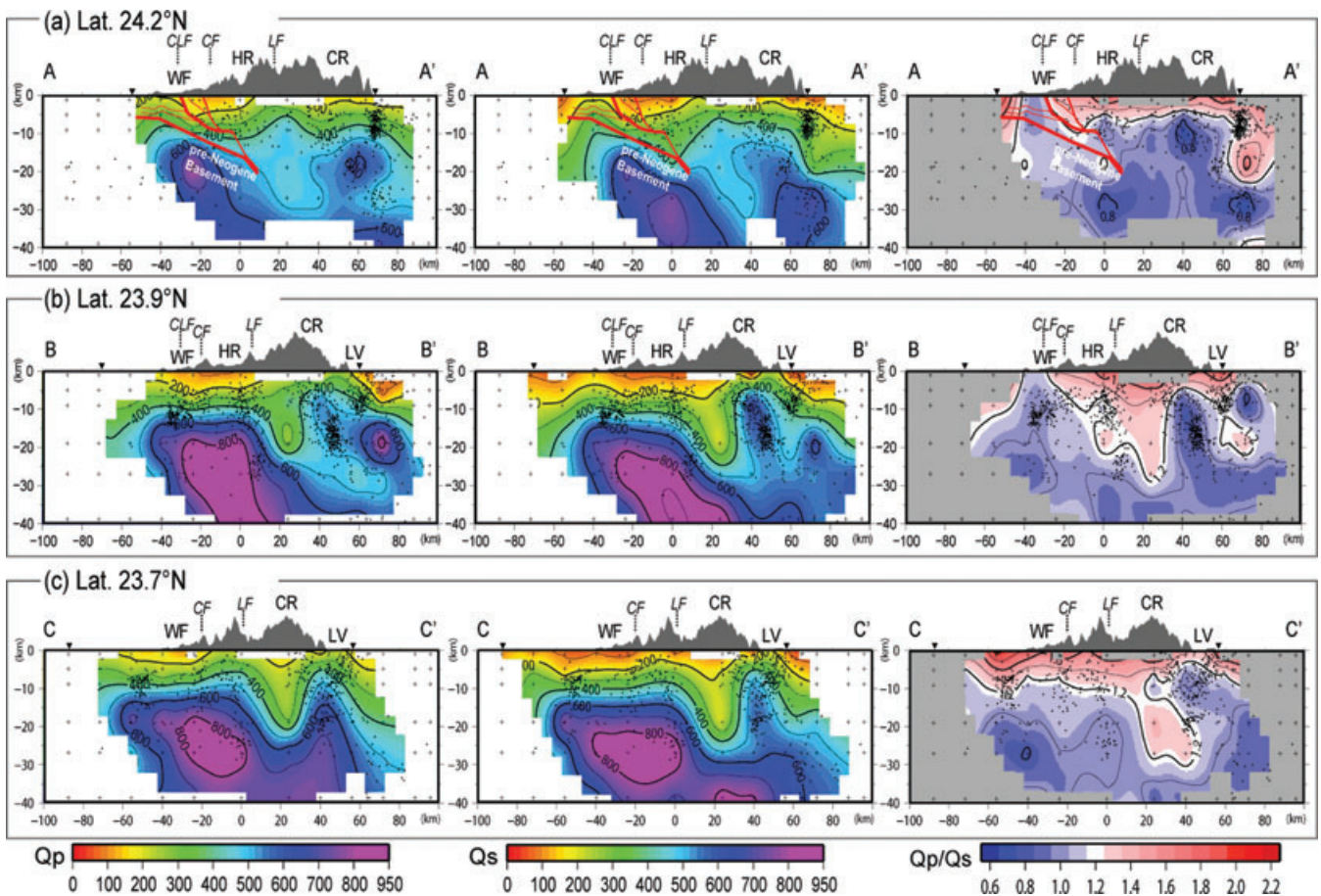
Figure 10. The *Qp* (left), *Qs* (middle) and *Qp/Qs* (right) profiles of (a) *AA'*, (b) *BB'* (c) *CC'*. The corresponding latitude of each profile with topography is also shown. The locations of each profile are denoted in Fig. 1(b). The red lines in profile *AA'* delineate the tectonic structure across the Chelungpu Fault (Wang *et al.* 2000). The background seismicity (dots) within 5 km of each profile for the period of 1991–2007 and grid nodes (crosses) are also shown. The contour interval of *Qp* and *Qs* images is 100, and is 0.2 for *Qp/Qs* images. The triangles at tops of each section denote the coastline. The abbreviations mark the location of tectonic features (Fig. 1a). The scale of vertical to horizontal is 2:1 shown by kilometres.

CCF. There are also high *Qs* at depths of 27 and 39 km with a longer block parallel to the CR. In synthetic test model II, we consider the inverted results of this study as the synthetic input model (Fig. A3).

Chelungpu Fault

The CLF system has been delineated by Wang *et al.* (2000) from a seismic experiment as shown by red lines in Fig. 10(a), in agreement with the geometry proposed by Mouthereau *et al.* (2001), with an upper décollement located in the upper cover strata and a lower décollement within the basement or at the basement–cover interface. Thus, we compare the images of *Qp*, *Qs* and *Qp/Qs* shallower than 20 km depth. A significant variation in *Qp*, *Qs* and *Qp/Qs* across the CLF is identified at shallow depth. The *Q* difference between the hangingwall and footwall is about 85 in *Qp* and 110 in *Qs*. Near the pre-Neogene basement at depths of about 8–10 km, the across-fault difference becomes less significant for both *Qp* and *Qs*. The *Qp/Qs* ratio of 1.2 aligns well with the identified CLF at depth from the seismic experiment (Wang *et al.* 2002), confirming that the observed contrast between hangingwall and footwall for *Qp* and *Qs* is associated with the CLF. Both of our synthetic tests show that the fault structure could be well retrieved as exhibited by the strong *Qs* contrast seen in Figs A1 and A3.

The strong contrast of attenuation properties across the CLF shows the existence of lithologic heterogeneity between the hangingwall and footwall. As the data we analysed cover the time period of the 1999 Chi-Chi earthquake sequence, and as the data for the time period before the 1999 Chi-Chi earthquake are not sufficient for the analysis, we cannot discern whether this strong contrast became more distinct due to the recent thrust movement of the ruptured CLF. However, our results are well correlated with the fault geometry obtained from seismic explosion experiment (Wang *et al.* 2002), geological observation and subsurface data (Mouthereau *et al.* 2001; Yue *et al.* 2005), GPS modelling (Hsu *et al.* 2002) and seismic modelling of the Chi-Chi earthquake (Lee *et al.* 2007).

Peikang High

The images along the profiles show distinct high *Qp* and *Qs* features at 9–19 km depth, especially for profiles *BB'* and *CC'* (Figs 10b and c), which also exhibit low *Qp/Qs*. This appears to correspond to the pre-Neogene basement, which is related to the strong barrier of the PH structure, as pre-Miocene basement extends from Penghu Islands to western Taiwan (Lin *et al.* 2003). In the orogenic evolution of Taiwan, the PH plays an important role as a stiff crustal obstacle, in the western continental margin, limiting
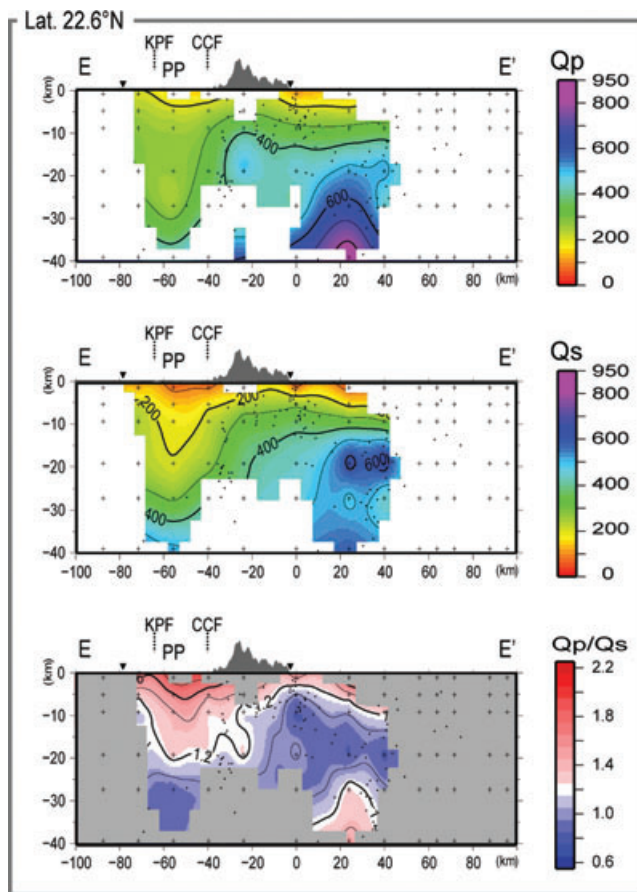
Figure 11. The *Qp* (top panel), *Qs* (middle panel) and *Qp*/*Qs* (bottom panel) profiles of *EE′*. The corresponding latitude of each profile with topography is also shown. The locations of the profile are denoted in Fig. 1(b). The background seismicity (dots) within 5 km of each profile for the period of 1991–2007 and grid nodes (crosses) are also shown. The contour interval of *Qp* and *Qs* images is 100 and is 0.2 for *Qp*/*Qs* images. The triangles at tops of each section denote the coastline. The abbreviations mark the location of tectonic features (Fig. 1a). The scale of vertical to horizontal is 2:1, shown by kilometres.

the advance of the tectonic wedge and hence exerts a major control on the development of the geometry of the fold-and-thrust belt (Lu *et al.* 1995; Mouthereau *et al.* 2002; Mouthereau & Lacombe 2006). The geodetic velocities (Yu *et al.* 1997) and seismicity are insignificant in the PH (Wang *et al.* 2000), which strongly contrasts with the larger geodetic deformation and high seismicity to the east. The distinctly east-dipping high *Qp* and *Qs* extensions are similar to the high *Vp* features in the velocity model (Cheng 2000) and are consistent with the seismic strong barrier by confining the earthquake distribution to depths less than about 50 km (Wang *et al.* 2000). The PH appears as a coherent east-dipping feature to 39 km depth in section *BB′*. In synthetic tests, a high *Qs* at PH was successfully recovered to the resolution limit of 39 km depth, but within limited spatial resolution only to the latitude of 24°N (Fig. A1d). Thus, we infer that the whole 100-km-long high Qs feature, imaged at 19 km depth (Fig. 9d), potentially extends to 39 km depth dipping to the east under the CR.

The strong and rigid properties of the PH might play a role in crustal deformation by giving a strong block that concentrates strain on its boundary. Mouthereau *et al.* (2009) studied the strain rate distribution in the Taiwan orogenic belt. They show that the maximum shear strain rate was to the east of CLF at 15–20 km

depth, which is well correlated with the high *Qp* and *Qs* at that depth (Figs 8d and 9d). At greater depth, the western boundary of high strain rate outlined the distribution of high *Qp* and *Qs* with values larger than 800 (Figs 8e and 9e). It seems to suggest that, in the upper crust, this major tectonic discontinuity is related to the kinematics of the CLF.

Central Range

In contrast to the east-dipping high *Qp*, and *Qs* images in western Taiwan, the apparent low *Qp* and low *Qs* feature beneath the CR to about 20–30 km depth is shown in the profiles *BB′* and *CC′* (Figs 10b and c). The zone with low *Qp* and *Qs* has the *Qp*/*Qs* ratio of about 1.2–1.4. It suggests relatively lower values in *Qs* within this zone compared to others. This zone also corresponds to the aseismic zone from seismological observations (Wang *et al.* 1994; Ellwood *et al.* 1996; Ma *et al.* 1996; Lin 1998).

Considering the velocity properties, the aseismic zone is within a low *Vp*/*Vs* region, with *Vp*/*Vs* around 1.6 (Kim *et al.* 2005; Wu *et al.* 2007), relative to the surrounding regions (*Vp*/*Vs* ∼ 1.73). Winkler & Nur (1982) suggested that the difference in two ratios of *Vp*/*Vs* and *Qp*/*Qs* could be related to different saturation of rocks. The *Qp*/*Qs* ratio larger than 1.0 might be related to the dry rock or the fully saturated rock. And for the fully saturated rock, *Vp*/*Vs* ratio could be larger than 2.0. Our high *Qp*/*Qs* (1.2–1.4) and low *Vp*/*Vs* (1.6) observed in the aseismic zone suggest that there is less opportunity that the aseismic zone is fluid related. Another observation is contributed by the magnetotelluric studies (Bertrand *et al.* 2009), which did not show a low resistivity anomaly under the CR, as would have been expected for fluid. Rather than fluid, another interpretation for the high *Qp*/*Qs* is temperature. For increasing temperature of rock, the values of *Qp* and *Qs* will be decreased, whereas *Qp*/*Qs* increased (Sanders *et al.* 1995). The results from our study suggest the significant role of temperature, as this aseismic zone has been related to high thermal anomalies and ductile properties in other recent interpretations based on velocity tomography (Kim *et al.* 2005) and thermal modelling (Lin 2000; Simoes *et al.* 2007; Yamato *et al.* 2009). The correspondence we show suggests that increased temperature yields the low *Qs* values, and also results in the aseismic zone. In the synthetic test, the CR low *Qs* is resolved to 27 km depth, although with less amplitude than the input model, suggesting that the observed low *Qs* could actually represent even lower *Qs* values (Figs A2b and c). More detailed discussion on the association of the attenuation structure to the thermal model beneath CR will be addressed in the later section.

Pingtung Plain

In addition to the contrast in *Qp* and *Qs* observed across the CLF, another significant across-fault contrast in *Qp* and *Qs* relates to the fault system in the PP as shown in Fig. 11. This feature is well resolved, as shown in the synthetic test (Fig. A2d). The PP is considered to be a foredeep related to the Manila Trench subduction zone (Biq 1977; Yu & Chiang 1997). To the west, it is bounded by the N10°E trending escarpment of the buried Kaoping Fault (KPF), and from the south by the WF. To the east, a major N–S trending fault, the Chaochou Fault (CCF), separated it from the CR (Angelier 2009). This valley was mainly filled with unconsolidated coastal and estuarine sediments of more than 5 km thickness (Chiang *et al.* 2004). The change in rock properties is distinctly exhibited beneath the PP, as the sharp lateral gradient of *Qp*, *Qs* and

Qp/Qs bracketed by these two faults. The *Qs* value of about 200 and high *Qp/Qs* of about 1.2–1.4 are identified and extend to around 20 km depth. The low *Qp*, *Qs* and high *Qp/Qs* together with high *Vp/Vs* value (Wu *et al.* 2007) characterize the fully fluid-saturated material (Winkler & Nur 1982; Hauksson & Shearer 2006) within this zone.

The previous *Qp* and *Qs* study of Lees & Lindley (1994) showed that there is high attenuation in the hangingwall of the San Andreas Fault and the attenuation decreases with depth. In *Qs*, the attenuation of the hangingwall is more apparent than in *Qp*. Hauksson & Shearer (2006) concluded that some spatial variations in *Qp* and *Qs* could be related to across-fault differences, for the San Jacinto, Elsinore and San Andreas Faults. However, at greater than 10 km depth, their observed variations within the *Qp* and *Qs* models appear to be less-fault controlled. In our study, the phenomenon can also be observed in the CLF and the faults surrounding the PP.

Comparison to tectonic models

To examine the correlation of the attenuation structure to proposed tectonic models, we made profiles *FF'* and *DD'* along the modelled sections of the thin-skinned model (Fig. 12a) of Suppe (1981), and the lithospheric collision model (Fig. 12b) of Wu *et al.* (1997). As *Qs* shows similar but more distinct features than *Qp*, we show the comparison only for the *Qs* images. In the thin-skinned model, tectonic deformation of plate collision results from the frontal accretion or underplating of the sediment cover above a main basal décollement with an east-dipping slope of 6°. The cross-section *FF'* (Fig. 1b) across central Taiwan, striking N110°E, shows that, to the west of the CR, the décollement as proposed by Suppe (1981) correlates with the *Qs* 400 contour line (Fig. 12a). The westward deepening of the décollement regionally is consistent with the thickening of crustal regions with low *Qs* values, suggesting that the weaker, thickened region of the hinterland is a major feature for the wedge-shaped orogen. However, in central and eastern Taiwan, the linear décollement shows less geometric concordance with downward deflection of *Qs* values.

The lithospheric collision model as proposed by Wu *et al.* (1997) suggests that both lithospheres of the Philippine Sea Plate and the Eurasian Plate were engaged in the Taiwan collision. This type of mountain building involves deformation of the whole crust, and even the upper mantle, rather than deforming only a thin wedge. For the *Qs* comparison, profile *DD'* incorporates the lithospheric collision model (Fig. 12b). A significant contrast of *Qs* structure beneath the WF and the CR was observed at 10–20 km depth. The low *Qs* value beneath the WF in the upper 10 km corresponds to the Neogene sediment layer. The identified aseismic crust zone of Wu *et al.* (1997) correlates well with a strong crust characterized by high *Qs* within 15–30 km depth beneath the WF and related to the PH. A thrust feature drawn in the lithospheric collision model aligns closely with a regime with high *Qs* values, which separates the low *Qs* regimes within the WF and the CR. Additionally, the trend of the *Qs* gradient from 10 to 30 km depth tends to coincide with the identified thrust feature. Another correlation is found for the thrust feature beneath the LV as a contour value of about 180, with lower *Qs* on the east, although the feature is limited by the resolution. This comparison suggests that the low *Qs* zone beneath the CR is associated with the extrusion of lower crust, for a region with ductile rheology (Wu *et al.* 1997; Mouthereau & Petit 2003) and concentrated high strain rates (Mouthereau *et al.* 2009). The low *Qs* region, which extends to 30 km depth, is shallower than Wu's inferred model of extrusion.
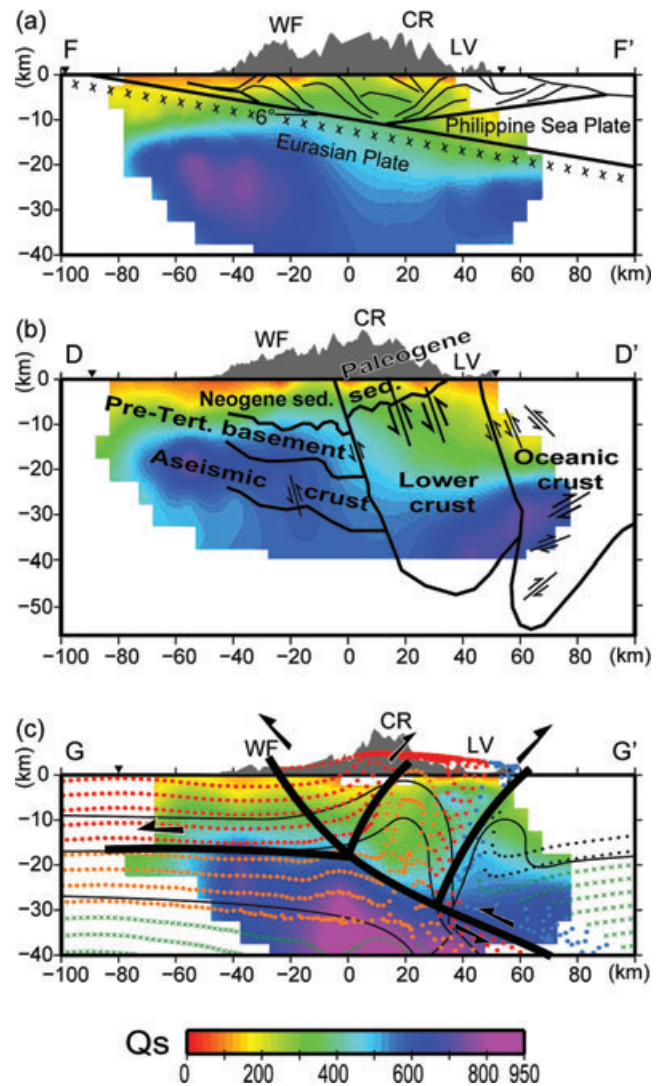
Figure 12. The comparison of *Qs* tomography to the tectonic models. The three models are (a) The thin-skinned model proposed by Suppe (1981), (b) the lithospheric collision model proposed by Wu *et al.* (1997) and (c) the thermal mechanical model proposed by Yamato *et al.* (2009).The extrusion behavior of the crust in the dynamic modelling is shown. The thick-lines mark main slip zones and the thin-lines illustrate the deformation of crust by shortening. The colour bar shows the values of *Qs* and the profiles correlated to the above models are *FF'*, *DD'* and *GG'*, respectively, as also denoted in Fig. 1(b). The abbreviations mark the location of tectonic features (Fig. 1a). The scale of vertical to horizontal is 2:1, shown by kilometres.

A quantitative tectonic model of central Taiwan has been developed recently. Yamato *et al.* (2009) presented a fully coupled thermomechanical numerical model of the Taiwan orogen development in which the mountain ranges result from the frontal accretion of the upper 25 km of rheologically layered continental margin crust. In detail, they indicated that, as an alternative to underplating modes of accretion below a shallow décollement, the orogenic wedge might involve a deep-seated flux of Eurasian continental margin middle-lower crust material to compensate for exhumation and erosion of the CR. Based on the analysis of seismogenic strain rates, Mouthereau *et al.* (2009) further identified that the ductile exhumation of the CR is associated with orogen-parallel extrusion. Profile *GG'* oriented N115°E (Fig. 12c) illustrates the comparison with the model of Yamato *et al.* (2009). The thermomechanical
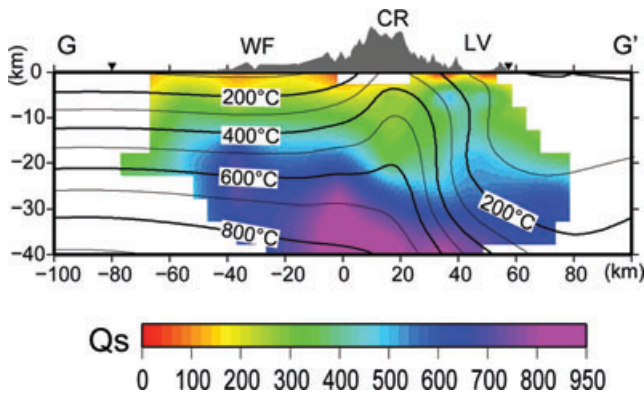
Figure 13. The comparison of *Qs* tomography to the thermal models by Yamato *et al.* (2009). The colour bar shows the values of *Qs* and the isotherm is shown by every 100 °C. The corresponding *Qs* profile was denoted in Fig. 1(b) as *GG′*. The abbreviations mark the location of tectonic features (Fig. 1a). The scale of vertical to horizontal is 2:1, shown by kilometres.

modelling shows the evolution of the upper continental crust (red dots), lower continental crust (orange dots) and the sediments of the former oceanic accretionary prism (blue dots). The oceanic crust (black stars) and the lithosphere mantle (green crosses) to the east are also presented. Our *Qs* image shows good correlation with the thermomechanical modelling under the WF, as the contour of *Qs* ~ 500 at 18 km depth corresponds to the boundary of the upper and lower continental crust. The high *Qs* of about 600 below this depth corresponds to the lower crust. As a result, the low *Qs* zone under the CR represents the exhumation of lower crust. Under the eastern edge of the CR, the upwarping of the high *Qs* feature also shows good correlation with the upper crust of the Eurasian margin. Fig. 12(c) shows significant correlation between the *Qs* distribution across Taiwan and the thermomechanical evolution of the Taiwan organic belt.

The thermal structures beneath the CR obtained by previous studies (Lin 2000; Simoes *et al.* 2007; Yamato *et al.* 2009) showed high temperature of about 350–500 °C at 10 km depth. To further relate the attenuation model to the thermal structure, we compare the *Qs* image with the constructed thermal model of Yamato *et al.* (2009) in Fig 13. It shows that the low *Qs* regime (high attenuation) beneath the CR at depths of 5–22 km is confined to the derived high temperature zone of 400–600 °C (Yamato *et al.* 2009). The temperature difference at this depth is about 100–150 °C compared to the corresponding depth in the adjacent WF and the difference in *Qs* is about 150. Our synthetic tests imply that the *Qs* difference could be even greater as there is smoothing across the low and high *Qs* anomalies (Figs A2b and c). It is notable that the wavelength of the derived thermal anomaly well coincides with the wavelength of the observed low *Qs* zone beneath the CR.

CONCLUSIONS

The comprehensive well-resolved *Qp*- and *Qs*-tomography exhibits the capability to image major structural features of Taiwan. The spatial variation in *Qp*- and *Qs*-tomography reflects heterogeneity bounded by the fault systems. The significant contrast between the hangingwall and footwall across the recently ruptured CLF shows across-fault differences in *Qp* and *Qs* values of 85 and 110, respectively. The ratio of *Qp/Qs* of 1.2 delineated the corresponding fault geometry. The Chaochou and Kaoping Faults, surrounding the PP, also exhibit remarkable across-fault contrast in *Qp* and *Qs*.

Beneath the CR, a significant region of low *Qp* and *Qs* extends downward to about 30 km. This high attenuation zone coincides well with the observed aseismic zone beneath the CR and is related to elevated temperature. The shear-wave attenuation image correlates well with the thermal structure from numerical models showing high temperature up to 600 °C at 20 km depth that corresponds to *Qs* values of about 350. The correspondence between the attenuation and thermal models suggests that the mountain building processes in Taiwan involve the deformation of the Eurasian lower crust. Thus, the low *Qs* feature beneath the CR is interpreted to be related to high temperature caused by lower crust exhumation. As such, our results better support collisional tectonic models with restricted subduction of the Eurasian crust (e.g. Wu *et al.* 1997; Lin *et al.* 1998; Yamato *et al.* 2009). Where there is adequate resolution, the attenuation model shows correlation with the location of active tectonic structure and helps differentiate between fluid and thermal effects. Thus, the attenuation model, especially *Qs*, illuminates different characteristics than velocity and provides new geophysical insights towards a better understanding of the Taiwan orogeny.

REFERENCES

Aki, K., 1967. Scaling law of seismic spectrum, *J. geophys. Res.,* **72,** 1217–1230.

Allen, R.V., 1978. Automatic earthquake recognition and timing from single traces, *Bull. seism. Soc. Am.,* **68,** 1521–1532.

Angelier, J. *et al.,* 2009. Does extrusion occur at both tips of the Taiwan collision belt? Insights from active deformation studies in the Ilan Plain and Pingtung Plain regions, *Tectonophysics,* **466,** 356–376.

Bertrand, E. *et al.*, 2009. Magnetotelluric evidence for thick-skinned tectonics in central Taiwan, *Geology,* **37,** 711–714.

Biq C., 1977. The Kenting melange and the Manila trench, *Proc. geol. Soc. China,* **20,** 119–122.

Chemenda, A.I., Mattauer, M., Malavieille, J. & Bokun, A.N., 1995. A mechanism for syn-collision rock exhumation and associated normal faulting: results from physical modelling. *Earth planet. Sci. Lett.,* **132,** 173–182.

Chen, K.C., 1995. Earthquake studies using the PANDA and PANDAII seismic array, *PhD thesis.* CERI/Dep. of Geol. Sci., Univ. of Memphis, Memphis, TN, USA.

Chen, K.J., 1998. S-Wave attenuation structure in the Taiwan area and its correlation to seismicity, *Terr. Atmos. Ocean.,* **9,** 97–118.

Chen, K.J., Yeh, Y.H. & Shyu, C.T., 1996. *Qp* structure in the Taiwan area and its correlation to seismicity, *Terr. Atmos. Ocean.,* **7,** 409–429.

Chen, K.P., 1998. Study of shallow structure beneath Kaoshiung–Pingtung region using local earthquake data, *PhD thesis.* Inst. of Geophys., Natl. Central Univ., Jungli, Taiwan.

Cheng, W.B., 2000. Three-dimensional crustal structure around the source area of the 1999 Chi-Chi earthquake in Taiwan and its relation to the aftershock locations, *Terr. Atmos. Ocean.,* **11,** 643–660.

Chiang, C.S., Yu, H.S. & Chou, Y.W., 2004. Characteristics of the wedge-top depozone of the southern Taiwan foreland basin system, *Basin Res.,* **16,** 65–78.

Drouet, S., Souriau, A. & Cotton, F., 2005. Attenuation, seismic moments, and site effects for weak-motion events: application to the Pyrenees, *Bull. seism. Soc. Am.,* **95,** 1731–1748.

Eberhart-Phillips, D. & Chadwick, M., 2002. Three-dimensional attenuation model of the shallow Hikurangi subduction zone in the Raukumara Peninsula, New Zealand, *J. geophys. Res.,* **107,** doi:10.1029/2000JB000046.

Eberhart-Phillips, D., Reyners, M., Chadwick, M. & Stuart, G., 2008a. Three-dimensional attenuation structure of the Hikurangi subduction zone in the central North Island, New Zealand, *Geophys. J. Int.,* **174,** 418–434.

Eberhart-Phillips, D., Chadwick, M. & Bannister, S., 2008b. Three-dimensional attenuation structure of central and southern South Island, New Zealand, from local earthquakes, *J. geophys. Res.,* **113,** doi:10.1029/2007JB005359.

Ellwood, A., Wang, C.Y., Teng, L.S. & Yen, H.Y., 1996. Gravimetric examination of thin-skinned detachment vs basement-involved models for the Taiwan orogen, *J. geol. Soc. China,* **39,** 209–221.

Geller, R.J., 1976. Scaling relations for earthquake source parameters and magnitudes, *Bull. seism. Soc. Am.,* **66,** 1501–1523.

Hauksson, E. & Shearer, P.M., 2006. Attenuation models (Q_P and Q_S) in three dimensions of the southern California crust: inferred fluid saturation at seismogenic depths, *J. geophys. Res.,* **111,** 1–21.

Hsu, S.K., Liu, C.S., Shyu, C.T., Liu, S.Y., Lallemand, S. & Wang, C., 1998. New Gravity and magnetic anomaly maps in the Taiwan-Luzon region and their preliminary interpretation, *Terr. Atmos. Ocean.,* **9,** 509–532.

Hsu, S.K., Yeh, Y.C., Lo, C.L., Lin, A.T. & Doo, W.B., 2008. Link between crustal magnetization and earthquakes in Taiwan, *Terr. Atmos. Ocean. Sci.,* **19,** doi:10.3319/TAO.2008.19.5.000 (T).

Hsu, Y.J., Bechor, N., Segall, P., Yu, S.B., Kuo, L.C. & Ma, K.F., 2002. Rapid afterslip following the 1999 Chi-Chi, Taiwan earthquake, *Geophys. Res. Lett.,* **29,** doi:10.1029/2002GL014967.

Kim, K.H., Chiu, J.M., Pujol, J., Chen, K.C., Huang, B.S., Yeh, Y.H. & Shen, P., 2005. Three-dimensional V_P and V_S structural models associated with the active subduction and collision tectonics in the Taiwan region, *Geophys. J. Int.,* **162,** 204–220.

Lee, S.J., Chen, H.W. & Ma, K.F., 2007. Strong ground motion simulation of the 1999 Chi-Chi, Taiwan earthquake from a realistic three-dimensional source and crustal structure, *J. geophys. Res.,* **112,** doi:10.1029/2006JB004615.

Lees, J.M. & Lindley, G.T., 1994. Three-dimensional attenuation tomography at Loma Prieta: inversion of t^* for Q, *J. geophys. Res.,* **99,** 6843–6863.

Lin, A.T., Watts, A.B. & Hesselbo, S.P., 2003. Cenozoic stratigraphy and subsidence history of the South China Seamargin in the Taiwan region, *Basin Res.,* **15,** 453–478.

Lin, C.H., 1998. Tectonic implications of an aseismic belt beneath the Eastern Central Range of Taiwan: crustal subduction and exhumation, *J. geol. Soc. China,* **41,** 441–460.

Lin, C.H., 2000. Thermal modeling of continental subduction and exhumation constrained by heat flow and seismicity in Taiwan, *Tectonophysics,* **324,** 189–201.

Lin, C.H., Yeh, Y.H., Yen, H.Y., Chen, K.C., Huang, B.S., Roecker, S.W. & Chiu, J.M., 1998. Three-dimensional elastic wave velocity structure of the Hualien region of Taiwan: evidence of active crustal exhumation, *Tectonics,* **17,** 89–103.

Lu, C.Y., Angelier, J., Chu, H.T. & Lee, J.C., 1995. Contractional, transcurrent, rotational and extensional tectonics: examples from northern Taiwan, *Tectonophysics,* **246,** 129–146.

Ma, K.F., Wang, J.H. & Zhao, D., 1996. Three-dimensional seismic velocity structure of the crust and uppermost mantle beneath Taiwan, *J. Phys. Earth,* **44,** 85–105.

Malavieille, J., Lallemand, S., Dominguez, S., Deschamps, A., Lu, C.Y., Liu, C.S., Schnürle, P. & Crew, A.S., 2002. Arc-continent collision in Taiwan: new marine observations and tectonic evolution, in: *Geology and Geophysics of an Arc-Continent Collision, Taiwan, Republic of China,* Geological Society of America Special Paper 358, pp. 187–211, eds Byrne, T.B. and Liu, C.-S., Geol. Soc. Am., Boulder, CO, USA.

Marquardt, D.W., 1963. An algorithm for least-squares estimation of nonlinear parameters, *J. Soc. Ind. Appl. Math,* **11,** 431–441.

Michelini, A. & McEvilly, T.V., 1991. Seismological studies at parkfield. I. Simultaneous inversion for velocity structure and hypocenters using cubic b-splines parameterization, *Bull. seism. Soc. Am.,* **81,** 524–552.

Mouthereau, F., Angelier, J. & Lee, J.C., 2001. Le séisme du 21 Septembre 1999: influence de l'héritage structural et implication du socle au front de la chaîne de Taiwan, *Comptes-Rendus de l'Académie des Sciences de Paris,* **333,** 93–103.

Mouthereau, F., Deffontaines, B., Lacombe, O. & Angelier, J., 2002. Variations along the strike of the Taiwan thrust belt: basement control on structural style, wedge geometry, and kinematics, in: *Geology and Geophysics of an Arc-Continent Collision, Taiwan, Republic of China,* Vol. 358: Geological Society of America Special Paper, pp. 35–58, eds. Byrne, T.B. and Liu, C.-S., GSA, Boulder, CO, USA.

Mouthereau, F., and Lacombe, O., 2006. Inversion of the Paleogene Chinese continental margin and thick-skinned deformation in the Western Foreland of Taiwan, *J. Struct. Geol.,* **28,** 1977–1993.

Mouthereau, F., Petit, C., 2003. Rheology and strength of the Eurasian continental lithosphere in the foreland of the Taiwan collision belt: constraints from seismicity, flexure and structural styles, *J. geophys. Res.,* **108,** 2512, doi:10.1029/2002JB002098.

Mouthereau, F., Fillon, C. & Ma, K.F., 2009. 3D distribution of strain rates the Taiwan orogenic wedge, *Earth planet. Sci. Lett.,* **284,** 361–385.

Rau, R.J. & Wu, F.T., 1995. Tomographic imaging of lithospheric structures under Taiwan, *Earth planet. Sci. Lett.,* **133,** 517–532.

Roecker, S.W., Yeh, Y.H. & Tsai, Y.B., 1987. Three-dimensional P and S wave velocity structures beneath Taiwan: deep structure beneath an arc-continent collision, *J. geophys. Res.,* **92,** 10 547–10 570.

Sanders, C.O., Ponko, S.C., Nixon, L.D. & Schwartz, E.A., 1995 Seismological evidence for magmatic and hydrothermal structure in Long Valley caldera from local earthquake attenuation and velocity tomography, *J. geophys. Res.,* **100,** 8311–8326.

Scherbaum, F., 1990. Combined inversion for the three-dimensional Q structure and source parameters using microearthquake spectra, *J. geophys. Res.,* **95,** 12 423–12 438.

Simoes, M., Avouac, J.P., Beyssac, O., Goffe, B., Farley, K.A. & Chen, Y.G., 2007. Mountain building in Taiwan: a thermokinematic model, *J. geophys. Res.,* **112,** B11450, doi:10.1029/2006JB004824.

Shyu, J.B.H., Sieh, K., Chen, Y.G. & Liu, C.S., 2005. Neotectonic architecture of Taiwan and its implications for future large earthquakes, *J. Geophys. Res.,* **110,** doi:10.1029/2004JB003251.

Suppe, J., 1980. Imbricated structure of western foothills belt, south-central Taiwan, *Petrol. Geol. Taiwan,* **17,** 1–16.

Suppe, J., 1981. Mechanics of mountain building and metamorphism in Taiwan, *Mem. geol. Soc. China,* **4,** 67–89.

Toomey, D.R. & Foulger, G.R., 1989. Tomographic inversion of local earthquake data from the Hengill-Grensdalur central volcano complex, Iceland, *J. geophys. Res.,* **94,** 17 497–17 510.

Trnkoczy, A., 1998. Understanding and setting STA/LTA trigger algorithm parameters for the K2, Application Note.

Thurber, C. & Eberhart-Phillips, D., 1999. Local earthquake tomography with flexible gridding, *Comput. Geosci.,* **25,** 809–818.

Walsh, J., 1995. Seismic attenuation in partially saturated rock, *J. geophys. Res.,* **100,** 15 407–15 424.

Wang, C., Huang, T.H., Yen, I.C., Wang, S.L. & Cheng, W.B., 2000. Tectonic environment of the 1999 Chi-Chi earthquake in central Taiwan and its aftershock sequence, *Terr. Atmos. Ocean.,* **11,** 661–678.

Wang, C., Huang, C.P., Ke, LY., Chien, W.J., Hsu, S.K., Shyu, C.T. & Cheng, W.B., 2002. Formation of the Taiwan Island as a solitary wave along the Eurasian continental plate margin: magnetic and seismological evidence, *Terr. Atmos. Ocean.,* **13,** 339–354.

Wang, C.Y., Chang, C.H. & Yen, H.Y., 2000. An Interpretation of the 1999 Chi-Chi Earthquake in Taiwan based on the thin-skinned thrust model, *Terr. Atmos. Ocean.,* **11,** 609–630.

Wang, C.Y., Li, C.L. & Yen, H.Y., 2002. Mapping the northern portion of the Chelungpu fault, Taiwan by shallow reflection seismics, *Geophys. Res. Lett.,* **29,** 37–31.

Wang, J.H., Chen, K.C. & Lee, T.Q., 1994. Depth distribution of shallow earthquakes in Taiwan, *J. geol. Soc. China,* **37,** 125–142.

Wang, Z., Zhao, D., Wang, J. & Kao, H., 2006. Tomographic evidence for the Eurasian lithosphere subducting beneath south Taiwan, *Geophys. Res. Lett.,* **33,** L18306, doi:10.1029/2006GL027166.

Wen, K.L., Chien, W.Y. & Chang Y.W., 2005. Unusual site effect analysis of the strong motion station in Taiwan (in Chinese), *Seism-tecchnical Report of MOTC-CWB* **39,** pp. 131–166.

Winkler, K.W. & Nur, A., 1982. Seismic attenuation: effects of pore fluids and frictional-sliding, *Geophysics,* **47,** 1–15.

Wu, F.T., Rau, R.J. & Salzberg, D., 1997. Taiwan orogeny: thin-skinned or lithospheric collision?, *Tectonophysics,* **274,** 191–220.

Wu, Y.M., Chang, C.H., Li Zhao, Shyu, J.B.H., Chen, Y.G., Sieh, K. & Avouac, J.P., 2007. Seismic tomography of Taiwan: improved constraints from a dense network of strong motion stations, *J. geophys. Res.,* **112,** B08312, doi:10.1029/2007JB004983.

Yamato, P., Mouthereau, F. & Burov, E., 2009. Taiwan mountain building: insights from 2D thermo-mechanical modelling of a rheologically-stratified lithosphere, *Geophys. J. Int.,* **176,** 307–326.

Yen, H.Y., Yeh, Y.H. & Wu, F.T., 1998. Two-dimensional crustal structures of Taiwan from gravity data, *Tectonophysics,* **17,** 104.

Yu, H.S. & Chiang, C.S., 1997. Kaoping shelf: morphology and tectonic significance, *J. Asian Earth Sci.,* **15,** 9–18.

Yu, S.B., Chen, H.Y. & Kuo, L.C., 1997. Velocity field of GPS stations in the Taiwan area, *Tectonophysics,* **274,** 41–59.

Yue, L.F., Suppe, J. & Hong, J.H., 2005. Structural geology of a classic thrust belt earthquake: the 1999 Chi-Chi earthquake Taiwan (Mw = 7.6), *J. Struct. Geo.,* **27,** 2058–2083.

APPENDIX A: SYNTHETIC TESTS

To verify the attenuation variation of significant structures that we interpret, two synthetic tests were made to evaluate the features of the Qs results. Synthetic tests, following Eberhart-Phillips *et al.* (2008a,b), demonstrate how well the tectonic features are resolved and how they are smeared by the data distribution. Synthetic t^* data were computed through the test model, then 3-D test inversions were carried out using the same damping parameters and initial models as the original inversions.

The synthetic test models incorporate simple shapes to examine: (1) the sharp variation across the CLF, and KPF and CCF which bounds PP at the depths of 1 and 19 km; (2) the low Qs of the CR aseismic zone at 19 km depth and (3) high Qs features at the depths of 27 and 39 km. In synthetic test model I (Fig. A1), low

Qs ($Qs = 50$) blocks were set east of CLF at 1–9 km depth and at the aseismic zone under CR at 19–27 km depth. In southwestern Taiwan, the synthetic test model also had a low Qs in PP bounded by KPF and CCF. There are also high Qs blocks at the depths of 27 and 39 km with a longer block parallel to the CR. The test inversion (Figs A1 and A2) showed that the overall Qs features of the discussed structures, such as CLF, PP and low Qs under CR were resolved with strong Qs contrast. For the CLF, the contrast of the hangingwall and footwall is seen in the Fig. A1(a) and in the profile (Fig. A2a). In the PP, the location and size of low Qs feature was illustrated clearly (Fig. A2d). For the high Qs features referring the PH at 27–39 km depth, we set a long high Qs features along the CR (Fig. A1c). The synthetic inversion had less capability to obtain the accurate shape along the strike of CR. The resolvable regime is concentrated in the central part of CR. The dipping aspect of this structure was also less resolved in Fig. A2(c), but is adequately imaged in section *BB'*. The results from synthetic test model I suggest that the identified features for CLF, and PP and low Qs in aseismic zone under CR in our Qs-tomography were well resolved. However, the high Qs feature related to the PH was only well resolved for the region to the south of 24°N, not well resolved for the northern profile.

We also make the synthetic test model II (Fig. A3) by using our inverted inversion result as an initial model. The inversion results for the synthetic tests are shown together at the corresponding depths and profiles in Figs A3 and A4. The spatial patterns are obtained by the inversion. Below 19 km depth, the recovered anomalies show reduced amplitude relative to the synthetic model.

The synthetic test results exhibit identified features addressed earlier in the text, but with less heterogeneity. The CLF and PP were able to be identified at the depths of 1 and 9 km. The low Qs in the CR was also resolved for the depth of 19 and 27 km. The shape of the high Qs regime was again resolved for the region less than 24°N. Both of our synthetic tests show that the fault structures (CLF, KPF and CCF) could be well retrieved as exhibited by the strong Qs contrast seen in Figs A1 and A3. The existence of low Qs under the CR was also well represented at the depth of 19–27 km. Neighboring the aseismic zone, the high Qs as referred to PH was also successfully recovered by synthetic tests at the resolution limit to the depth at 39 km, but with limited spatial resolution, only to the latitude of 24°N (Fig. A1d).
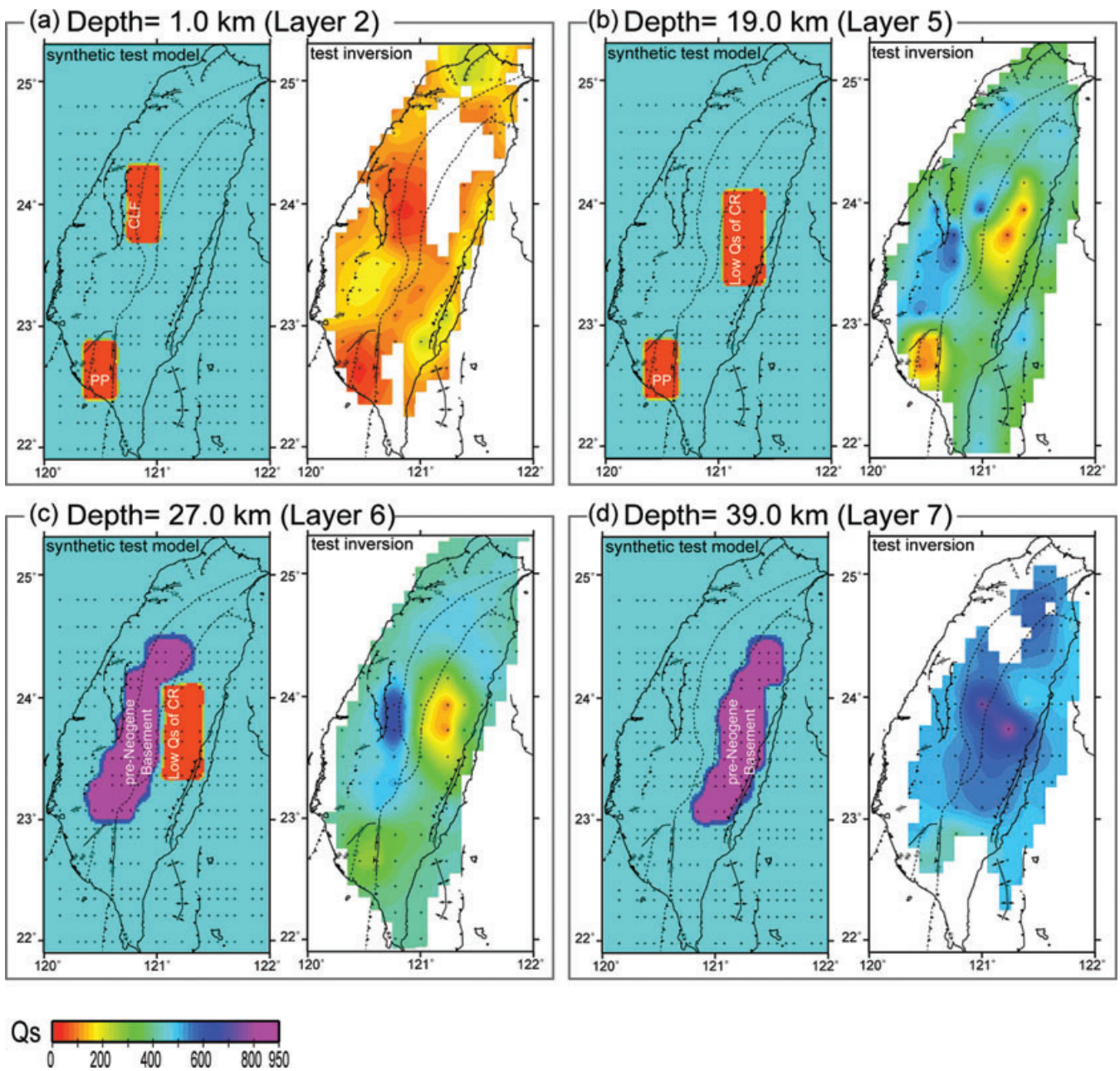
Figure A1. Synthetic test model I. The test models are shown on the left, whereas the inversions of the test models are shown on the right, accordingly, in the panels for depths of 1, 19, 27 and 39 km. The major tectonic features are shown (Fig. 1a). Crosses show the grid nodes, which allow sharp boundaries in the synthetic models relative to the inversion models.
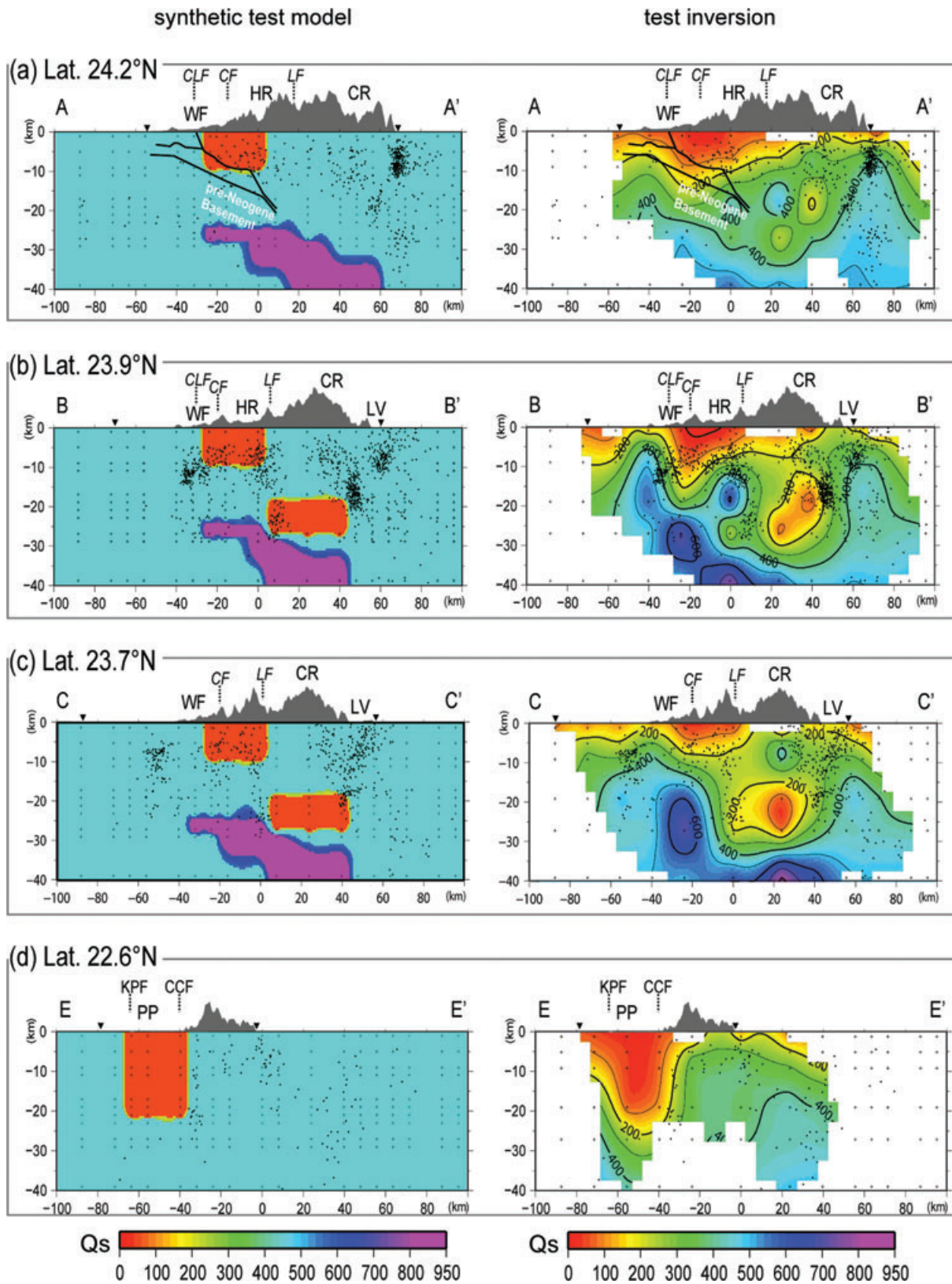
Figure A2. The latitudinal profiles of test model I (left-hand panel) and corresponding test inversion model (right-hand panel). Locations of the profile are denoted in Fig. 1(b). Background seismicity (dots), grid nodes (crosses), coastline locations, structure abbreviations are shown as in Fig. 11.
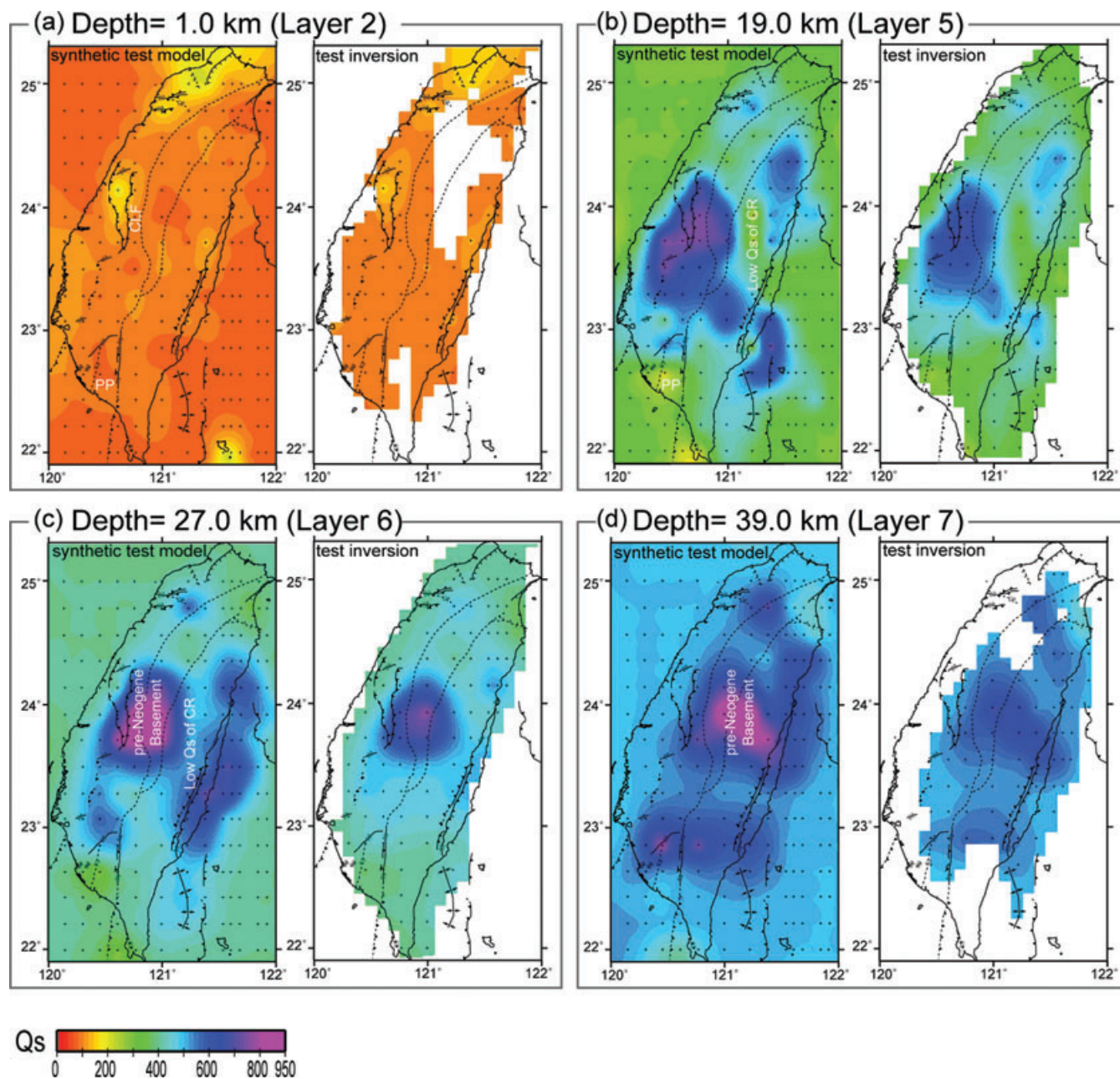
Figure A3. Synthetic test model II. The test models are shown on the left, whereas the inversions of the test models are shown on the right, accordingly, in the panels for depths of 1, 19, 27 and 39 km. The major tectonic features are shown (Fig. 1a). Crosses show the grid nodes.
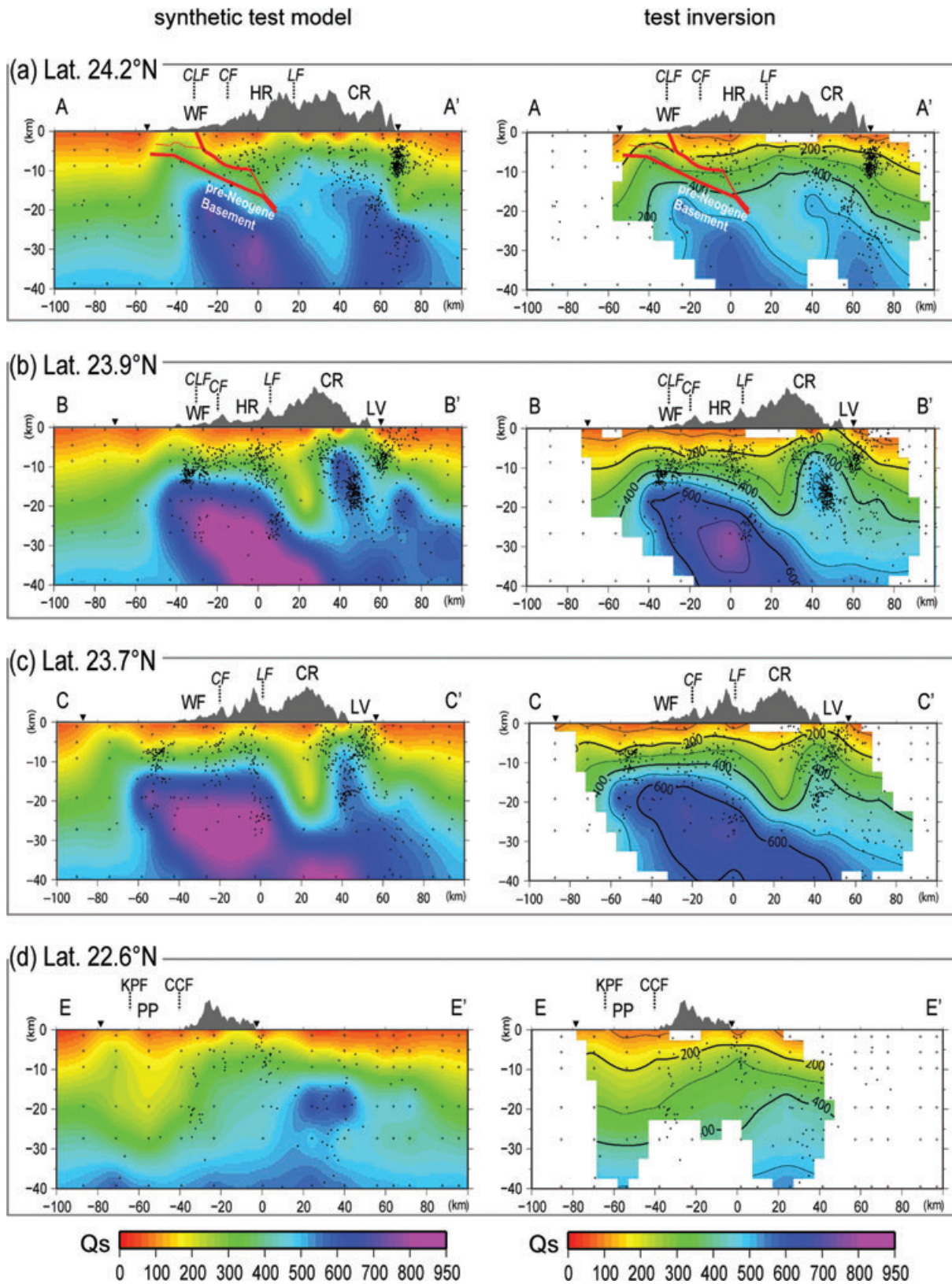
Figure A4. The latitudinal profiles of test model II (left-hand panel) and corresponding test inversion model (right-hand panel). Locations of the profile are denoted in Fig. 1(b). Background seismicity (dots), grid nodes (crosses), coastline locations, structure abbreviations are shown as in Fig. 11.